Hindawi
Advances in Civil Engineering
Volume 2021, Article ID 6671875, 22 pages
https://doi.org/10.1155/2021/6671875

Research Article

Effect of Congestion on Flow Field of Vented Natural Gas Explosion in a Kitchen

Lei Pang,[1,2] Qianran Hu,[1] Mengjie Jin,[1] and Kai Yang [1,2]

[1]*School of Safety Engineering, Beijing Institute of Petrochemical Technology, Beijing 102617, China*
[2]*Beijing Academy of Safety Engineering and Technology, Beijing 102617, China*

Correspondence should be addressed to Kai Yang; ycyangk@bipt.edu.cn

Received 14 October 2020; Revised 16 December 2020; Accepted 18 December 2020; Published 13 January 2021

Academic Editor: Qian Fang

The process of gas explosion venting in a typical Chinese civil kitchen was investigated using computational fluid dynamics technology, focusing on the impact of the scale and cross-sectional characteristics of congestion, such as common furniture and electrical appliances, on the explosion flow-field parameters. An asymmetrical distribution of congestion will cause the uneven combustion of explosion flames in the kitchen. The flame will initially spread on one side of the room and then accelerate toward the surrounding areas, thereby increasing the risk of indoor gas explosion. The typical indoor overpressure change process can be divided into five stages, among which Stage V is found to be related to pseudoclosed combustion. Large-scale congestion has an obstructive effect on the explosion flow field, but it changes under certain conditions, while small-scale congestion only acts as a promoter. The flat congestion cross section helps maintain the stability of the flame structure, whereas the continuous and abrupt change of the congestion cross section can induce strong turbulent combustion. The research results provide a theoretical basis for the prevention and control of natural gas explosion hazards in civil kitchens from the perspective of congestion scale and cross-sectional mutation.

1. Introduction

Problems such as aging gas pipelines, damaged valves, and irregular operation have led to the increased incidence of urban gas deflagration accidents, which pose a serious threat to building structures and personal safety [1]. In 2019, there were 463 indoor gas explosion accidents in China, 301 of which occurred in households, accounting for 65% of the total. Civil gas explosion accidents usually occur in the kitchen and mainly involve natural gas explosions. The influence of restraint conditions on gas explosions is extremely significant [2, 3]. A natural gas explosion in the kitchen will not only develop into a restrained explosion venting process because of the effects of doors and windows but also be affected by congestion, such as furniture and electrical equipment. Congestion of different sizes and uneven placement will increase the turbulence of the indoor flow field, accelerate the propagation of turbulent flames, and further aggravate the complexity of the transient flow field of natural gas explosions in the kitchen [4, 5]. Therefore, studying the influence of congestion on the explosion venting characteristics of natural gas in the kitchen is of great significance for reducing the threat posed by such accidents.

In the past few decades, an increasing number of scholars have used experimental and numerical methods to carry out a large number of studies on large-scale confined spaces with built-in congestion gas explosions and explosion venting effects [6]. Moen et al. [7] used a 50 m^3 circular pipe to study the effects of the area blocking rate and amount of orifice congestion on the explosion venting of a methane/air mixture. They found that a relatively small repetitive congestion will significantly increase the explosion overpressure in the pipeline. Harrison and Eyre [8] used a 4000 m^3 container to carry out methane/air and propane/air explosion venting experiments. Studies have found that reducing the height of the congestion array or the blockage of each grid of the array can significantly inhibit flame acceleration and overpressure growth.

Diakow et al. [9] used a 392 m^3 explosion container to study the effects of small-scale array congestion in a propane/air explosion venting experiment, with the congestion arranged in the second half of the chamber. They found that the peak pressure inside the container decreased with the decrease in the volume blockage rate. Bauwens et al. [10] explored the effects of the congestion array on propane explosion venting through a 63.7 m^3 explosion chamber. They found that the unburned gas bypassed the congestion and increased the indoor turbulence intensity; the flame surface area also increased. Chen et al. [11] analysed the influence of the arrangement of gas cylinder congestion on hydrogen explosion using a 27 m^3 room. They found that the maximum indoor overpressure and flame speed induced by double-layer congestion were higher than those of single-layer congestion. Zhang et al. [12] used numerical methods to study the influence of the arrangement of congestion on a propane/air vented explosion and analysed the progression of disasters, such as indoor and outdoor overpressure and high temperature under the action of congestion. Tomlin et al. [13] explored the impact of small-scale array congestion on methane/air explosion venting through a 182.25 m^3 chamber. They found that when the flame passes through the second congestion array, its front continues to accelerate and compete with the downstream congestion interacts, thereby causing turbulence to establish a positive feedback mechanism. Skjold et al. [14] explored the impact of different sizes and arrangements of congestion on the hydrogen vented explosion process in a 33 m^2 container. They found that a high blocking rate would cause a shift from deflagration to detonation. Chao et al. [15] established a prediction model for the maximum indoor explosion overpressure under the effect of congestion, which required the estimation of the maximum indoor flame area.

Table 1 summarises the relevant details of the congestion characteristics in the literatures [7–13]. It can be seen that the volume blocking rate studied by scholars does not exceed 7%, while the maximum volume of a single congestion does not exceed 1 m^3. Although these studies have clarified the process of gas explosion in large-scale rooms and considered the influence of factors, such as the blocking rate, shape, quantity, and arrangement of congestion on the overpressure hazard, the relevant research results are insufficient to guide the design of antiexplosion civil kitchens. The main problems are as follows:

(1) In civil kitchens, the geometric scales of congestion, such as furniture and electrical equipment, are usually large, which means that a higher blocking rate will be formed in the room; however, small-scale congestion is mainly considered in existing research.

(2) The congestion in kitchens is generally placed along the walls on both sides, and the congestion distribution is asymmetrical, which causes a sudden change in congestion at the cross section of the room. The complex arrangement of congestion will have an important impact on the explosion flow field. However, existing research has focused on regular and evenly spaced arrays of congestion.

(3) Owing to the effects of large-scale complex congestion, exploring the evolution mechanism of the local flow field plays an important role in understanding the development process of gas explosion disasters. However, existing large-scale vented explosion studies focus on the impact of congestion on explosion overpressure and flame. At the same time, small-scale vented explosion research cannot be directly used to guide large-scale explosion disaster control.

Taking the natural gas vented explosion in a typical civil kitchen as the research object, this paper examines the effect of large-scale continuous asymmetrical indoor congestion on the dynamic evolution process of the explosion flow field, such as the flame, overpressure, and turbulence, with the help of computational fluid dynamics (CFD) technology. It analyses the influence of congestion scale and the congestion characteristics of an abrupt cross section on the restraint vented explosion. It summarises the effects of different congestion characteristics on the flow field before and after the vented explosion to provide a scientific basis for the mechanism and prevention of such accidents.

2. Research Methods

2.1. Numerical Models. The simulation calculation in this paper adopts the same numerical model as literature [2]. The reliability of numerical model has been verified in the famous BFETS and MERGE experimental tests, and the numerical simulation results were in good agreement with the experimental results [16]. It has been widely used worldwide and is suitable for gas explosion and impact dynamics problems. Its PRESSURFS boundary condition can set a specific static opening pressure for a specific surface structure according to the actual situation to solve the transient flow field of explosion and explosion under limited space constraints [17]. The model mainly uses the finite volume method to solve a series of equations including mass-conservation equation, momentum-conservation equation, and energy-conservation equation. With the help of Cartesian tensor notation, it can be expressed as follows [18].

The mass-conservation equation is

$$\frac{\partial \rho}{\partial t} + \frac{\partial}{\partial x_j}\left(\rho u_j\right) = 0. \tag{1}$$

The momentum-conservation equation is

$$\frac{\partial}{\partial t}\left(\rho u_i\right) + \frac{\partial}{\partial x_j}\left(\rho u_j u_i\right) = -\frac{\partial p}{\partial x_i} + \frac{\partial \tau_{ij}}{\partial x_j}. \tag{2}$$

The energy-conservation equation is

Table 1: Details of congestion research on large-scale vented explosion.

Literatures	Chamber size (m)	Fuel	Congestion details		
			Shape	Maximum size (m)	Maximum V.B.R. (%)
Moen et al. [7]	$L = 10$, $D = 2.5$	Methane	Orifice plate	$L = 0.015$, $D = 2.5$	4.50
Harrison and Eyre [8]	$V = 4000\ \mathrm{m}^3$	Methane\propane	Cylindrical	$L = 8$, $D = 0.315$	0.40
Diakow et al. [9]	$14.63 \times 7.32 \times 3.66$	Propane	Cylindrical	$L = 3.66$, $D = 0.051$	0.50
Bauwens et al. [10]	$4.6 \times 4.6 \times 3$	Propane	Cuboid	$3 \times 0.4 \times 0.4$	6.00
Chen et al. [11]	$3 \times 3 \times 3$	Hydrogen	Cylindrical	$L = 1.45$, $D = 0.22$	4.00
Zhang et al. [12]	$4.6 \times 4.6 \times 3$	Propane	Cuboid	$3 \times 0.56 \times 0.56$	6.14
Tomlin et al. [13]	$9 \times 4.5 \times 4.5$	Methane	Cylindrical	$L = 4.6$, $D = 0.18$	5.00

L and D are the height and diameter of the cylinder, respectively, in m; V.B.R. is the volume blocking rate; V.B.R. is V_{ob}/V, where V_{ob} and V are the congestion and chamber volume, respectively, in m^3.

$$\frac{\partial}{\partial t}(\rho E) + \frac{\partial}{\partial x_j}\left(\rho u_j E\right) = \frac{\partial}{\partial x_j}\left(\Gamma_E \frac{\partial E}{\partial x_j}\right) - \frac{\partial}{\partial x_j}\left(p u_j\right) + \tau_{ij}\frac{\partial u_i}{\partial x_j}, \tag{3}$$

where x is the space coordinate, t is the time coordinate, ρ is the density, u is the velocity, p is the static pressure, and i and j are the coordinate directions. E is the specific internal energy; its expression is

$$E = C_v T + m_{\mathrm{fu}} H_c, \tag{4}$$

where C_V is the constant-volume specific heat, T is the temperature, m_{fu} is the mass fraction of the fuel, and H_c is the heat of combustion. The turbulent-diffusion coefficient is $\Gamma* = \mu_t/(\sigma)*$, where $(\sigma)*$ is the default value of the turbulent Prandtl constant. τ_{ij} is the viscous stress tensor; its expression is

$$\tau_{ij} = \mu_t\left(\frac{\partial u_i}{\partial x_j} + \frac{\partial u_j}{\partial x_i}\right) - \frac{2}{3}\delta_{ij}\left(\rho k + \mu_t \frac{\partial u_i}{\partial x_j}\right), \tag{5}$$

where the turbulence-viscosity coefficient $\mu_t = C_\mu \rho k^2/\varepsilon$, where k and ε are the turbulent kinetic energy and its dissipation rate, δ_{ij} is the Kronecker delta, and the value of the model constant C_μ is $0.09\ \mathrm{m}^2/\mathrm{s}$. The turbulence in the vented gas explosion process is described by the standard k-ε turbulence model. It consists of two conservation equations for k and ε, respectively:

$$\frac{\partial}{\partial t}(\rho k) + \frac{\partial}{\partial x_j}\left(\rho u_j k\right) = \frac{\partial}{\partial x_j}\left(\Gamma_k \frac{\partial k}{\partial x_j}\right) + \tau_{ij}\frac{\partial u_i}{\partial x_j} - \rho\varepsilon, \tag{6}$$

$$\frac{\partial}{\partial t}(\rho \varepsilon) + \frac{\partial}{\partial x_j}\left(\rho u_j \varepsilon\right) = \frac{\partial}{\partial x_j}\left(\Gamma_\varepsilon \frac{\partial \varepsilon}{\partial x_j}\right) + C_1 \frac{\varepsilon}{k}\tau_{ij}\frac{\partial u_i}{\partial x_j} - C_2 \frac{\rho \varepsilon^2}{k}, \tag{7}$$

where C_1 and C_2 are constants (C_1 and $C_2 = 1.44$ and 1.79). A one-step reaction model is used to describe the combustion process of the fuel/air mixture. This is mathematically formulated as a conservation equation for the fuel mass fraction:

$$\frac{\partial}{\partial t}(\rho m_{\mathrm{fu}}) + \frac{\partial}{\partial x_j}\left(\rho u_j m_{\mathrm{fu}}\right) = \frac{\partial}{\partial x_j}\left(\Gamma_{\mathrm{fu}} \frac{\partial m_{\mathrm{fu}}}{\partial x_j}\right) + R_{\mathrm{fu}}. \tag{8}$$

The volume combustion rate $R_{\mathrm{fu}} = C_t\ \rho\ (s_2^t/\Gamma_{\mathrm{fu}})\ R_{\min}$, where $R_{\min}$ is the minimum of the mass fractions for fuel, oxygen, and the reaction product, and C_t is the combustion-model constant ($C_t = 40$). The turbulence combustion velocity is expressed as

$$S_t = 1.8 u_t^{0.412} \cdot L_t^{0.196} \cdot S_l^{0.784} \cdot \nu^{-0.196}, \tag{9}$$

where u_t is the turbulence intensity, L_t is the characteristic length of the turbulence, S_l is the specific laminar combustion velocity, and ν is the fluid dynamic viscosity.

The effective laminar burning velocity S_b can be expressed as

$$S_b = S_l\left(1 + F_s R_f\right), \tag{10}$$

where S_l is the specific laminar combustion velocity, R_f is the spherical flame radius, F_s is the laminar flame acceleration coefficient, and the value is 0.15.

2.2. Verification of Grid Independence. The numerical model uses an eight-node structural grid to discretise the space and subgrid technology to describe the effect of small-scale entities on the flow field [19]. To investigate the influence of the grid size on the accuracy of capturing the explosion flow field, a room with a size of $3.4\ m \times 2.1\ m \times 2.4$ m with no congestion was selected as the research object. A square vented surface with a size of $0.8\ m \times 0.8$ m was provided on the smaller vertical wall of the room, and its opening pressure was set to 20 kPa. The room was filled with methane/air premixed gas at a concentration of 10% and in a static state; the ignition source was 0.05 m away from the back wall. For this physical model, two sets of sizes, $0.1\ m \times 0.1\ m \times 0.1$ m (M1) and $0.05\ m \times 0.05\ m \times 0.05$ m (M2), were used to mesh it. Table 2 shows the comparison of the peak overpressures of the two sets of grids. It can be seen that the relative discrepancy of the peak overpressure is within 9%, indicating that the two grid sizes have little influence on the calculation and can be applied to the present calculation [20]. To save time and improve calculation efficiency, the M1 grid was used in this study, and adaptive grid technology was used to automatically adjust the grid in certain areas to improve the accuracy of the numerical calculation.

Table 2: The comparison results of peak overpressure.

Distance to the back wall/m	P_{M1}/kPa	P_{M2}/kPa	Absolute discrepancy	Relative discrepancy/%
0.5	21.52	23.33	1.81	7.8
0.9	21.32	23.32	2.00	8.6
3.3	20.00	20.01	0.01	0
4.1	8.48	8.77	0.29	3.3
7.7	7.83	8.15	0.32	3.9

2.3. Experimental Validation of the Model. To verify the applicability of the selected numerical model, it was compared with the large-scale gas explosion experiment of Bauwens et al. [10]. Bauwens carried out an explosion study using an experimental device with dimensions of 4.6 m (length) × 4.6 m (width) × 3.0 m (height) to investigate the deflagration characteristics in the presence of eight medium-scale congestion objects (0.4 m × 0.4 m × 3.0 m); the volume blocking rate was 6%. The overpressure time curve was taken from the measuring point at the geometric centre on one side of the explosion chamber. This verification used the same parameter conditions as those in the experiment. Among them, the vented surface was made of a 0.02 mm thick polypropylene plastic film, and its static opening pressure was approximately 0.5 kPa. The four walls of the room as well as the ceiling and the floor were all adiabatic smooth rigid walls. The outside air is static. The initial ambient pressure and temperature were set to 1.01325×10^5 Pa and 300 K, respectively. The venting surface completely ruptures immediately after reaching its opening pressure. The ignition source was located at the geometric centre of the back wall and was 0.25 m away from the back wall.

Figure 1 shows the comparison of the explosion overpressure time curve between the experiment and numerical simulation. Table 3 compares the experimental and simulated peak overpressure and its arrival time. It can be seen that the relative discrepancy of the peak overpressure and arrival time between the experiment and numerical simulation was below 4% and that the trends of the overpressure time curve of both are similar. The numerical simulation restores the actual overpressure peak structure. Owing to the uncertainty of the experimental device, the accuracy of the sensor, and the experimental process, the error may be caused by a combination of factors, such as experimental test and computational domain dispersion [2]. In summary, it is feasible to solve the transient flow field problem of indoor gas vented explosions under congestion conditions using the above numerical methods.

3. Research Plan

Based on China's "Design Code for Residential Buildings" [21] and "National Building Standard Design Atlas-Residential Kitchen" (14J913-2) [22], this study selected an apartment kitchen with a type II structural layout as the research object [23], as shown in Figure 2. The survey found that the large-scale congestion in the kitchen usually includes counters, wall cabinets, refrigerators, and range hoods, which are generally arranged against both sides of the wall. Counters, refrigerators, and so forth are often placed on the floor along the wall, while wall cabinets and range hoods are hung against the wall (red-dotted line in Figure 2). The shape of congestion in the kitchen is usually a rectangle, whose three sides measure 0.3–0.7 m. The maximum length can penetrate the entire kitchen longitudinally (e.g., a row of cabinets, wall cabinets, etc.). The kitchen volume blocking rate is generally 10–35%. The above data will serve as the basis for the selection of typical congestion features in the physical model.

The physical model of the type II kitchen is shown in Figure 3. Based on the general size of a type II kitchen in Chinese civil residences, the model kitchen size was set as 3.4 m (length) × 2.1 m (width) × 2.4 m (height). Indoor congestion was set according to the general actual size (some objects that were custom-made and a special size were not be considered in this study). Wall cabinets, counter cabinets, refrigerators, and pipe wells are examples of large-scale congestion, while range hoods and water heaters can be considered as small-scale congestion. The sizes of these objects will not be described in detail. The kitchen volume blocking rate was 33.72%, excluding subtle structures, such as handles and decorative lines that may exist on the surface of some congestion. The walls, ceiling, floor, and congestion surfaces around the kitchen were all set as rigid walls, and the door in Figure 2 is equivalent to the back wall. With reference to the window size of an ordinary kitchen and the static opening pressure range of the glass, the window in Figure 2 is regarded as a square vent with a size of 0.8 m × 0.8 m; the lower edge is 1 m from the floor, and the opening pressure is 20 kPa. To accurately describe the impact of the external explosion on the indoor explosion flow field, the calculation domain was extended to five times the length of the room along the direction of the vent. The extended part of the calculation domain was set as a free flow boundary; the computational domain was discretised using the cube structure grid described above; and the time step was set to 1×10^{-5} s. The calculated domain size is 20 m × 2.1 m × 2.4 m, and the total number of grids generated by a grid size of 0.1 m is 115,575. The kitchen was filled with methane/air premixed gas with a volume concentration of 10% in a static state. The initial pressure and temperature of the environment in the calculation domain were set to 1.01325×10^2 kPa and 300 K, respectively. A spherical ignition source with a radius of 0.015 m was placed at the geometric centre position 0.05 m away from the back wall of the kitchen. To accurately describe the distribution and sudden change in the characteristics of the explosion flow field, several measuring

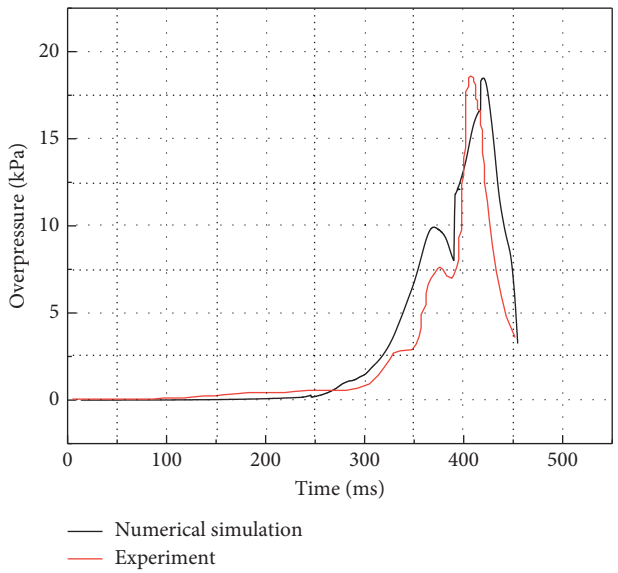

Figure 1: Comparison of explosion overpressure time curve between experiment and simulation (ignition at back wall; vent area is 5.43 m2).

Table 3: The comparison results between experiment and simulation.

Explosion parameters	Experiment	Simulation	Absolute discrepancy	Relative discrepancy/%
Peak overpressure (kPa)	18.60	18.48	0.12	0.65
Peak overpressure arrival time (ms)	407	420	13	3.10

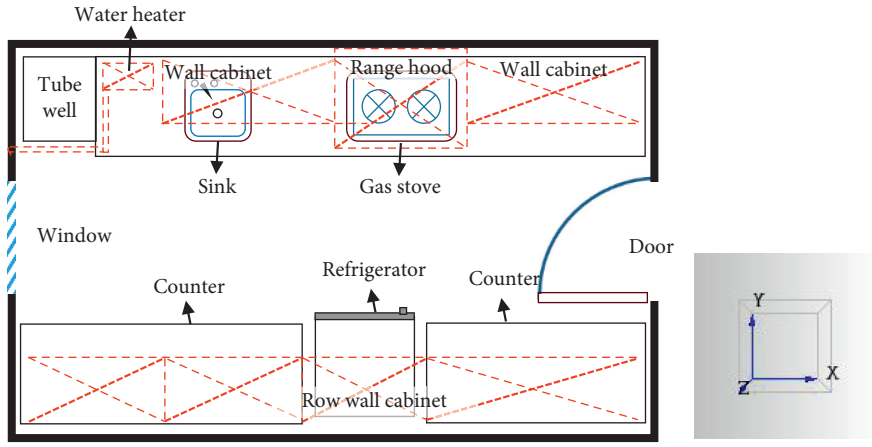

Figure 2: Layout of the type II kitchen.

points were set up in different indoor areas, as shown in Figure 4. Table 4 provides a detailed description of all the measuring points.

4. Results and Discussion

4.1. Typical Flow-Field Distribution Characteristics under the Action of congestion

4.1.1. Flame Propagation and Velocity Vector. The typical flame propagation and flow-field velocity vector cloud diagram after ignition are shown in Figure 5 (COMB.RATE is the combustion rate in kg/s, ABS.VELOCITY is the flow velocity vector in m/s, and the white-dashed line represents congestion). Figure 5(a) shows that the finger flame front moves forward steadily within 170 ms after ignition, and the axial and radial flame propagation speeds are basically the same. At 220 ms, the axial gas diffusion velocity induced by the opening of the vent increased, and the flame speed began to accelerate toward the vent. At this time, although the flame has made contact with the row wall cabinet, its front has not changed significantly. This is because the large-scale congestion is arranged close to the edge of the wall, and its long side is consistent with the direction of flame

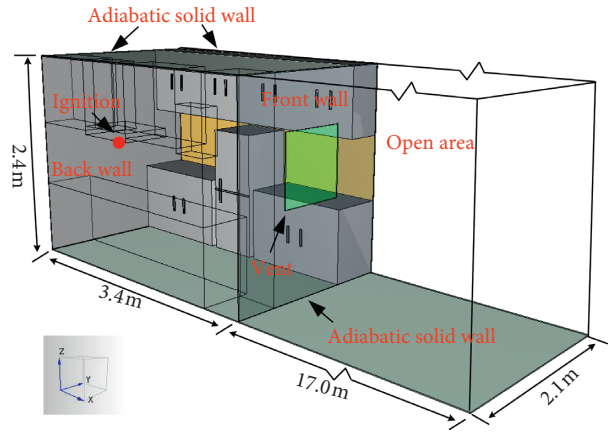

Figure 3: Physical model of the type II kitchen.

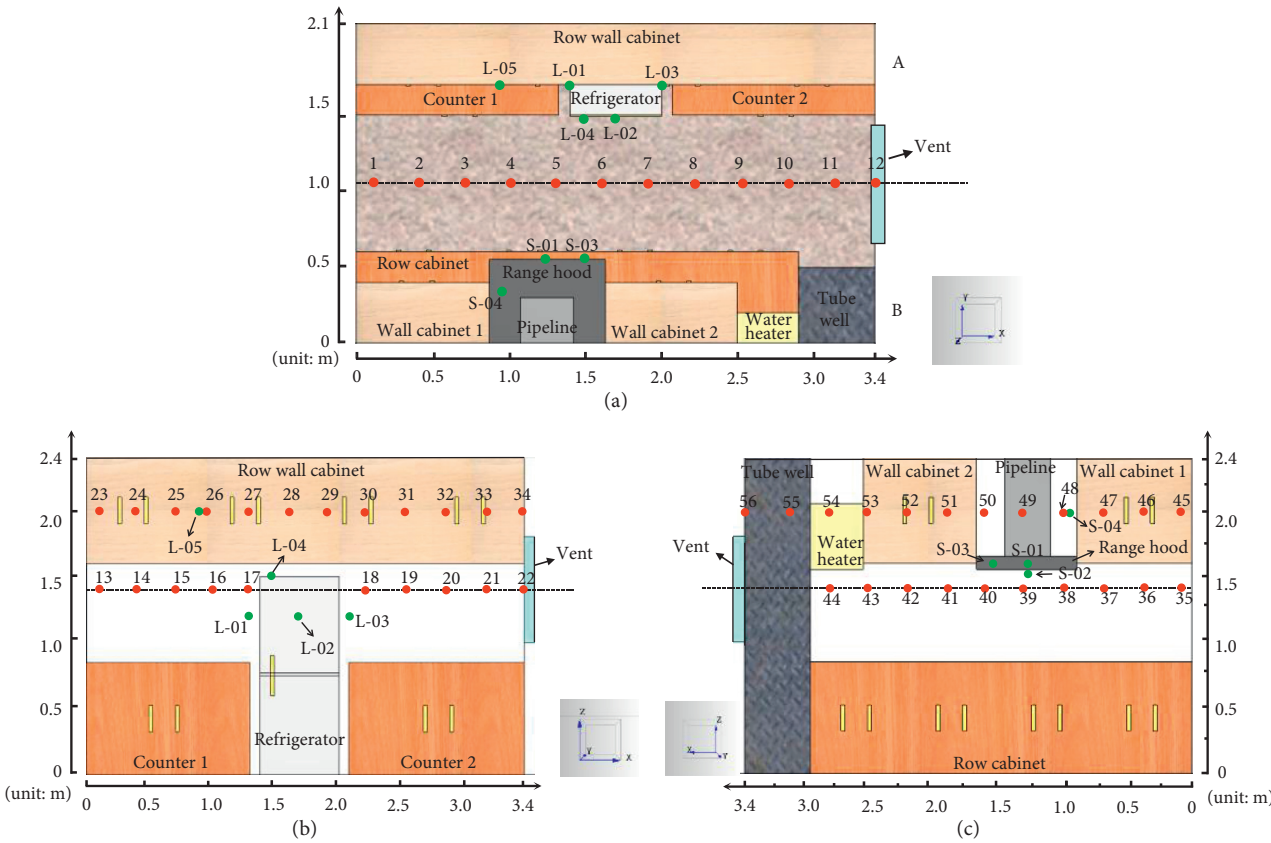

Figure 4: Specific layout of measuring points. (a) Physical model top view. (b) Part A. (c) Part B.

propagation. It does not cause additional obstruction and turbulence to the flame. The concentration of the methane-air mixture in the early stage of flame development is relatively high, and the flame front is not easily affected by fluid dynamics and diffusion instability [24]. Therefore, the flame continues to propagate at a laminar velocity. Figure 5(b) shows that almost all indoor gas flowed toward the vent, which proves the above process.

The congestion began to influence the flame structure at 270 ms. An elliptical flammable gas burning zone (COMB.RATE > 1.08 kg/s) appeared near the height of the range hood and quickly expanded to the surroundings (the gas began to flow toward both sides of the room in Figure 5(b)) and caught up with the flame front at 290 ms, resulting in a significant increase in flame structure thickness. Under the action of the flame expansion, the high-speed gas outflow area (ABS.VELOCITY > 108 m/s) gradually expanded from indoor to outdoor, and the gas flow velocity reached its maximum. The combustion intensity reached the maximum under the induction of vented

Table 4: The detailed description of measuring points.

Configuration	Gauges	Description
1	1–12	Arrange sequentially along the centre line of the vent ($y = 1.05$ m, $z = 1.4$ m)
2	13–22	Arranged along the x-axis at 0.6 m above the cabinets 1 and 2 ($y = 1.8$ m, $z = 1.4$ m)
3	23–34	The surface of the row wall cabinet is arranged in sequence along the x-axis ($y = 1.7$ m, $z = 2.0$ m)
4	35–44	Arranged along the x-axis at 0.6 m above the row cabinet ($y = 0.3$ m, $z = 1.4$ m)
5	45–56	Wall cabinets 1 and 2 are arranged in sequence along the x-axis ($y = 0.4$ m, $z = 2.0$ m)
6	L-01	The left centre surface of the refrigerator ($x = 1.4$ m, $y = 1.725$ m, $z = 1.2$ m)
	L-02	The front centre surface of the refrigerator ($x = 1.7$ m, $y = 1.425$ m, $z = 1.2$ m)
	L-03	The right centre surface of the refrigerator ($x = 2.0$ m, $y = 1.425$ m, $z = 1.2$ m)
7	S-01	The front centre surface of the range hood ($x = 1.25$ m, $y = 0.55$ m, $z = 1.6$ m)
	S-02	The bottom centre surface of the range hood ($x = 1.25$ m, $y = 0.275$ m, $z = 1.55$ m)
8	L-04	Near the top of refrigerator ($x = 1.5$ m, $y = 1.425$ m, $z = 1.6$ m)
	S-03	The surface of the range hood is close to wall cabinet 2 ($x = 1.5$ m, $y = 0.55$ m, $z = 1.6$ m)
9	L-05	Somewhere on the surface of the row wall cabinet ($x = 0.975$ m, $y = 1.7$ m, $z = 2$ m)
	S-04	In the gap between wall cabinet 1 and pipeline ($x = 0.975$ m, $y = 0.35$ m, $z = 2$ m)

Gauges in configurations 1–5 are all separated by 0.3 m (except gauges 17 and 18).

turbulence (310 ms). At 360 ms, a severe burning zone appeared in the depression area near the height of the water heater. At 420 ms, the burning gas was blocked by the congestion, and the ceiling, floor and other gaps continued to burn. At this time, the direction of the indoor gas flow was generally the same, but the flow velocity was greatly reduced, which is the final stage of the vented explosion.

In summary, the initial explosion flame remained stable as it developed along the long side of the congestion. Small-scale congestion triggered the indoor violent turbulent combustion phenomenon, thereby changing the flame propagation direction and distribution position of the explosion flame, which will result in a sharp increase in the degree of indoor disasters.

Figure 6 shows the flame development cloud diagram at different moments on the $x = 1.7$ m slice. Owing to the obstruction of the refrigerator and the turbulence produced by the range hood, the flame front first extends to the wall of the range hood. In the later stage of flame development, the combustion phenomenon occurs in the row of cabinets, wall cabinets, and refrigerators nearby. Under the combined effects of the different characteristics of congestion, the gas explosion flame distribution in the kitchen is irregular, and the development trend is complex.

4.1.2. Characteristics of Overpressure Formation and Flame Evolution. To explore the correlation between the overpressure dynamics and flame development, based on the general characteristics of restraining vented explosion overpressure development and through comparative analysis of the combustion rate (Figure 7(i)), mass flow (Figure 7 (ii)), and flame area (Figure 8), the overpressure time curve was divided into five stages, as shown in Figure 7(i). It can be seen that the overpressure does not rise significantly within 40 ms after ignition (Stage I), indicating that the flame is dominated by laminar burning. When the flame spreads to the surroundings, the combustion rate of flammable gas in the room increases, and the overpressure shows a rapid upward trend. The combustion rate does not change significantly in Stage II, indicating that the flame has not spread to this point. Stage III includes the Helmholtz oscillation caused by the vent opening and the flame accelerating toward the vent under the action of turbulence. At 210 ms, the opening of the vent causes the methane/air mixture near the vent to be quickly released under the pressure difference between the indoor and outdoor (peak P_b formation) [25], and the corresponding mass flow suddenly rises and reaches a peak. At the same time, the overpressure oscillation peak P_{hel} caused by the Helmholtz effect is formed with the opening of the vent [26]. At 262 ms, as the flame front expands, the rate of combustion product generation increases, causing the mass flow to increase again. However, the mass flow suddenly decreased at 295 ms, the combustion rate increased abruptly, and peak P_{ext} was formed [27]. In Stage IV, the overpressure, combustion rate, and mass flow all fluctuate for a short time near the maximum value and then suddenly decrease, which is mainly attributed to the maximum flame area caused by the refrigerator [28]. As shown in Figure 8(b), the flame propagates toward the wall at a faster speed at 316 ms. At this time, the flame area reaches its maximum, thus forming the peak P_{mfa}, until the flame area and mass flow begin to decrease, and the overpressure drops rapidly.

In Stage V, a weak pressure oscillation was observed. Based on previous studies [29], the pressure oscillation at the end of a vented explosion is believed to be caused by pseudoclosed combustion; that is, during the explosion flame venting process, an unburned gas and air mixture surrounded by hot burning gas will form in the room. The unburned gas will continue to expand after being heated and ignited by the surrounding burning gas, but its expansion will be restricted by the surrounding burning gas, congestion, and chamber walls. Figure 9 shows that when the flame accelerates toward the vent after ignition, the burning gas near the indoor ceiling, floor, and congestion is not completely exhausted, but a large amount of unburned gas, combustion products, and air mixture are retained. Residual burning occurs between the congestion and wall, forming pseudoclosed combustion [30].

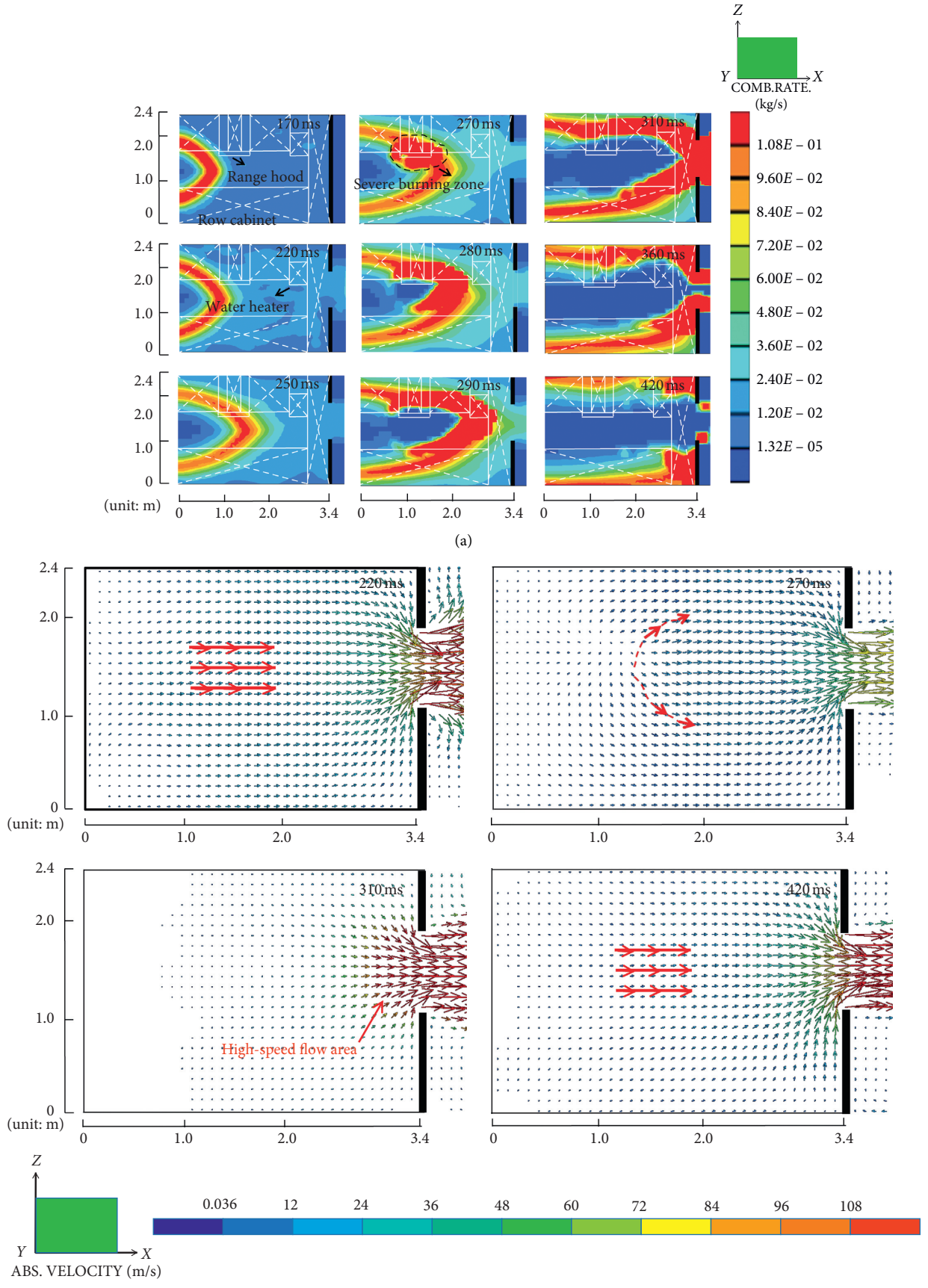

Figure 5: The change process of (a) flame propagation and (b) flow-field velocity vector on the $y = 1.05$ m slice after ignition.

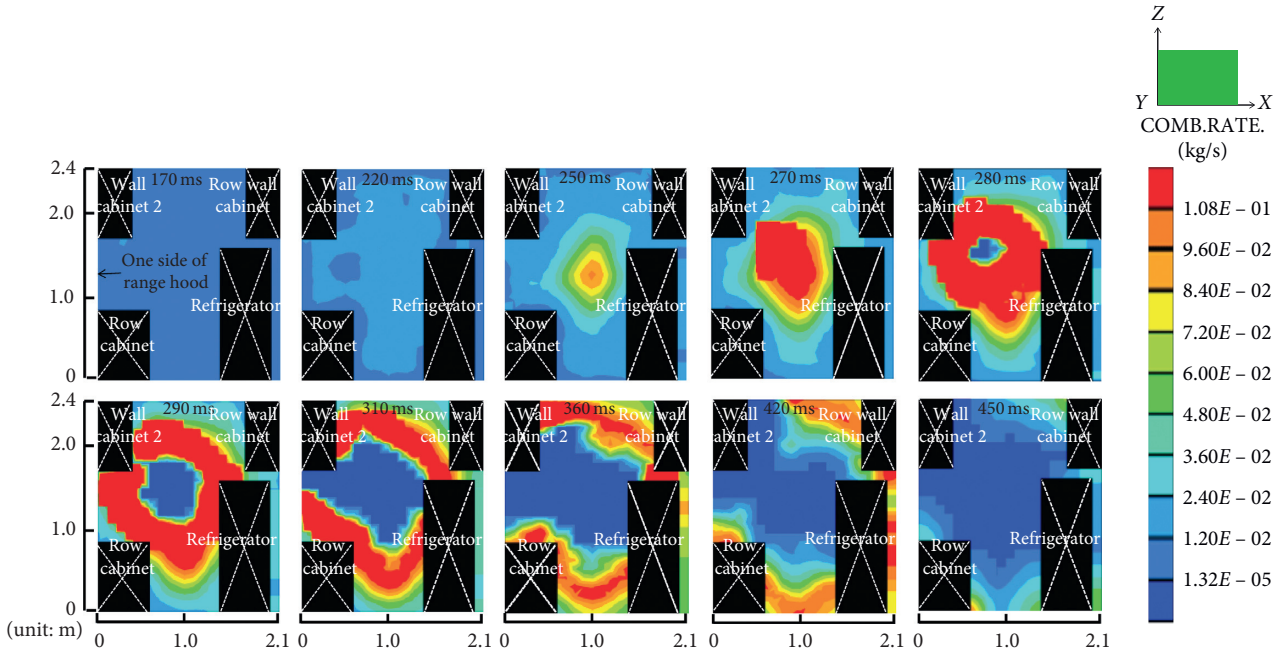

Figure 6: The flame expansion cloud diagram at different moments on the $x = 1.7$ m slice after ignition.

In summary, the overpressure change in Stage III is related to the gas release mass flow rate. The overpressure in Stage IV is closely related to the combustion rate, mass flow, and flame surface area. The oscillation in Stage V is affected by pseudoclosed combustion.

4.2. The Influence of congestion Size on Explosion Flow Field

4.2.1. The Law of Flame Propagation Induced by Characteristics of Congestion Size. To study the influence of the congestion size in the kitchen on the flame structure, Figure 10 compares the flame expansion cloud diagram on two paths: $y = 1.8$ m (configuration (2) and $y = 0.3$ m (configuration 4). Figure 11 compares the (a) peak combustion rate and (b) its arrival time, (c) overpressure time curve, (d) time trajectory of the flame front position, and (e) flame speed of the two paths.

It can be seen from Figure 10(a) that, within 280 ms, the flame front almost develops toward the refrigerator in a finger shape. The flame front position and propagation speed increase linearly, and the flame presents laminar burning before it propagates toward the refrigerator [31]. Therefore, the peak combustion rate is low before reaching the refrigerator, and its arrival time increases linearly. The pressure gradient formed on the surface of the refrigerator hinders the expansion of the hot burning gas and causes the accumulation of energy, which leads to a slight increase in local overpressure [32, 33]. With the expansion of the burning gas (280–300 ms), the unburned gas in front of the flame is forced to flow from the passage between the refrigerator and row wall cabinet. The vortex is generated by the interaction between the airflow and congestion and acts on the flame behind the congestion. This results in flame front deformation and a rapid increase in surface area [34, 35]. At this time, the combustion rate in Figure 11 has significantly increased, the burning time is shorter, and the overpressure increases. The flame front accelerates in the form of a partial jet, and the maximum propagation speed to the rear of the refrigerator can reach 140 m/s [35–37]. At 380 ms, the flame burn-out zone first appears at the initial formation position of the vortex, and the increase in flame speed leads to the expansion of the vortex intensity and area behind the refrigerator [38]. In Figure 11(e), the flame speed decreased sharply before approaching the front wall. This is because the flame is gradually restricted by the solid wall in the forward direction of the flame, and the gas flow velocity is gradually reduced [39].

For the path $y = 0.3$ m in Figure 10(b), a violent chemical reaction suddenly occurred near the range hood at 280 ms, and a burn-out zone appeared in the middle of the explosion flame after approximately 20 ms. The rapidly increasing combustion rate and shorter burning time in the range hood area in Figures 11(a) and 11(b) illustrate the above phenomenon. Small-scale congestion will induce the unburned gas at the flame front to form a larger and strong vortex, causing the flame to sharply accelerate from 17 m/s to 85 m/s as it approaches the range hood, and overpressure will follow the increase. After 310 ms, the flame burn-out zone continues to expand, but the lateral expansion speed is obviously greater than the radial speed. Compared with the surface of the row cabinet, the flame burn-out zone first appears in the congestion gap, which shows that, in the pseudoclosed combustion stage, the unburned gas mainly stays near the large-scale congestion and can burn continuously at low intensity.

In summary, the dual effects of congestion on the explosion flow field and conversion mechanism have gradually become clear. Flame propagation in front of a large-scale congestion is hindered, but its combustion rate and propagation speed increase significantly behind the congestion,

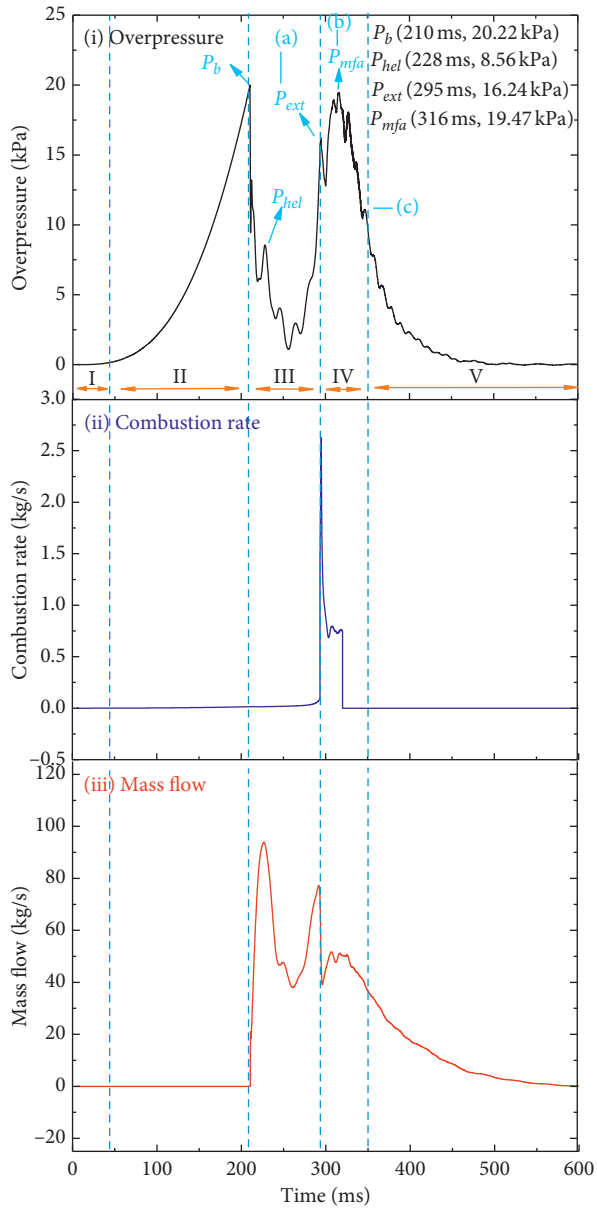

Figure 7: Time history curve of (i) overpressure, (ii) combustion rate, and (iii) mass flow near the vent (gauge 12).

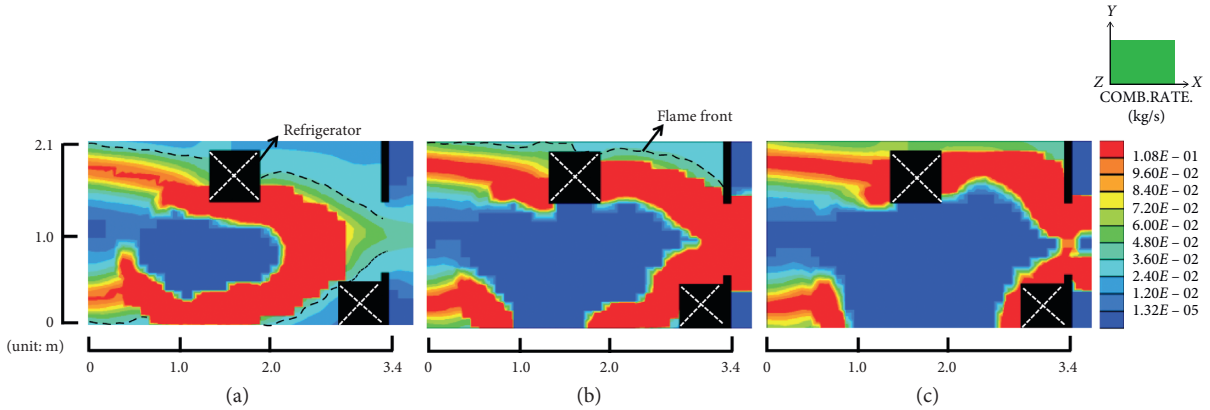

Figure 8: The expansion of explosion flame area at the moments of Figures 7(a)-7(c) on the $z = 1.4$ m slice (the black-dotted line is the flame front). (a) 295 ms. (b) 316 ms. (c) 349 ms.

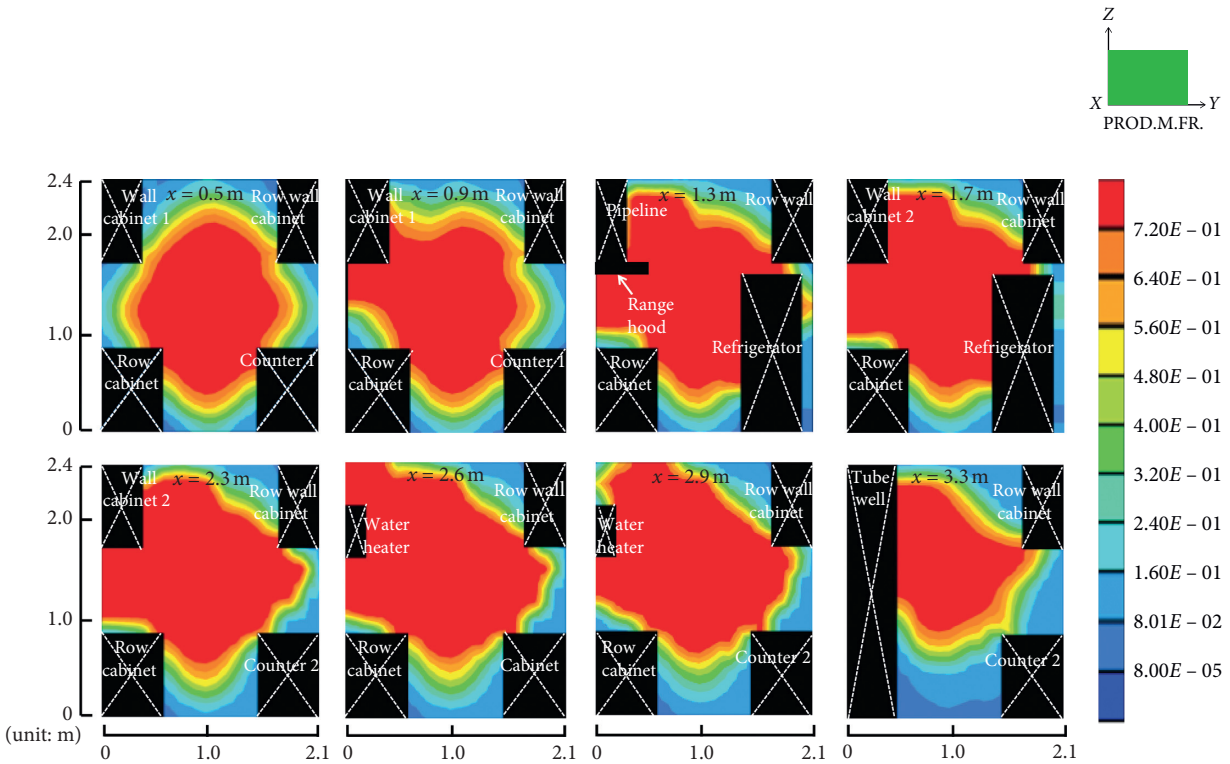

FIGURE 9: The reaction change process of different cross sections at $t = 374$ ms (the number on each cloud diagram is the distance to the back wall; PROD.M.FR is the mass fraction of combustion products).

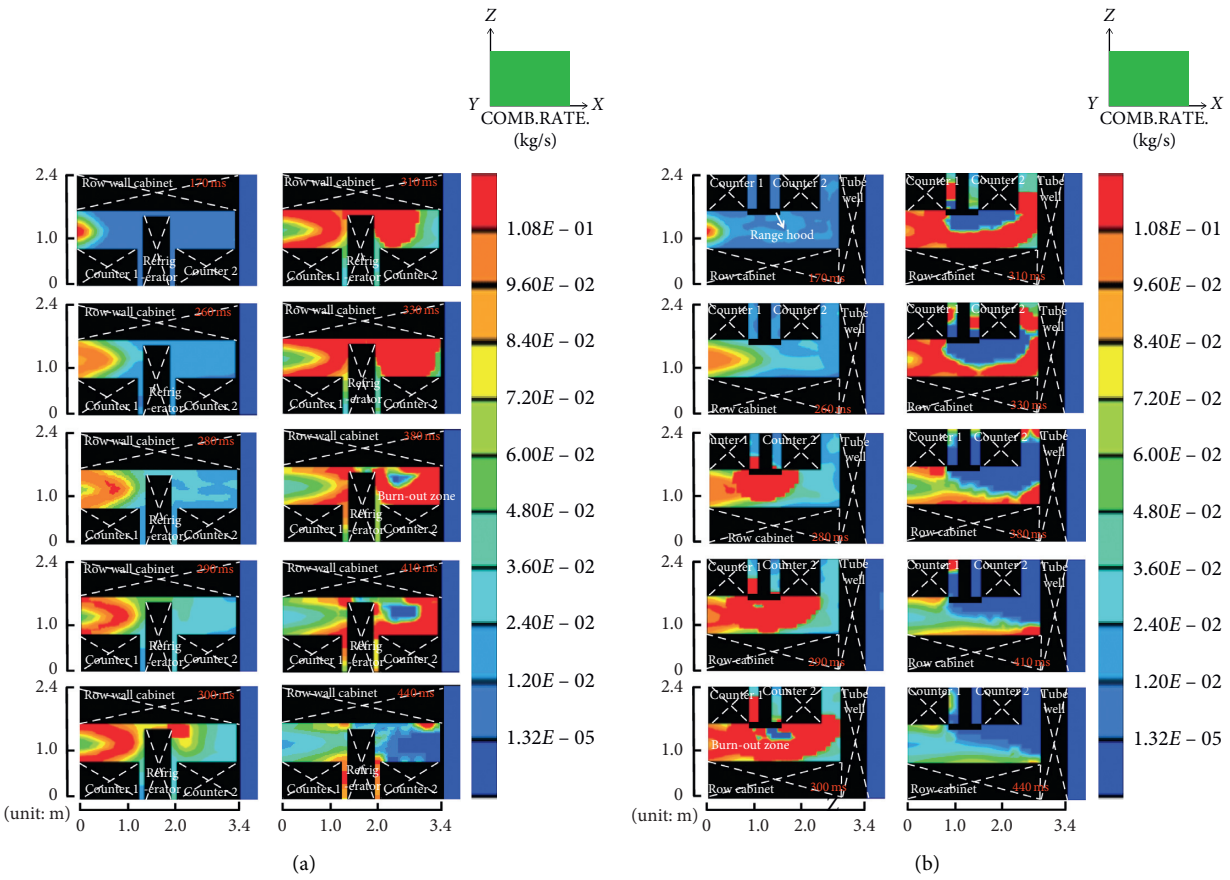

FIGURE 10: The flame expansion cloud diagram on the two paths $y = 1.8$ m and $y = 0.3$ m after ignition. (a) $y = 1.8$ m. (b) $y = 0.3$ m.

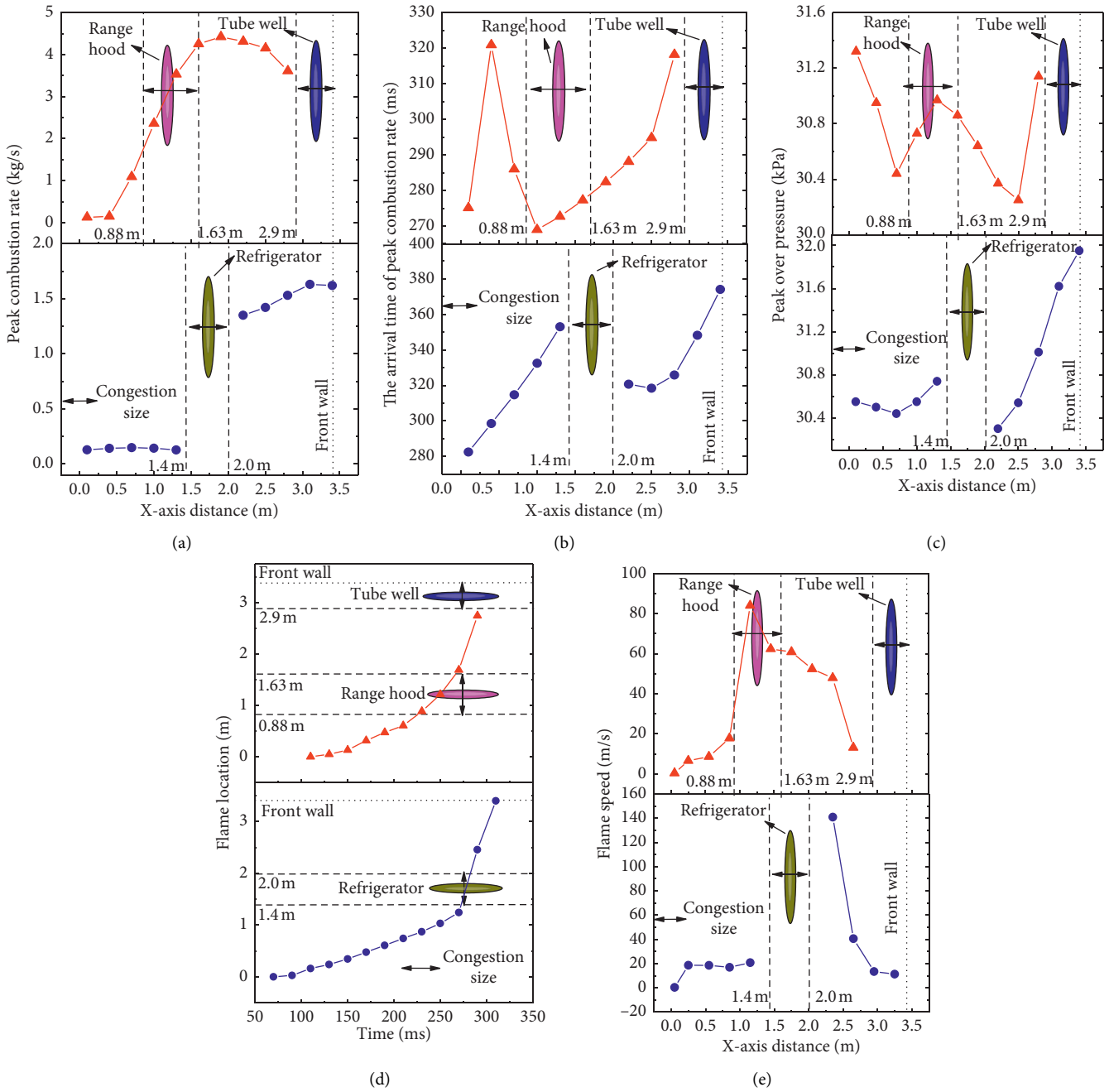

Figure 11: The variation law of (a) peak combustion rate and (b) arrival time, (c) overpressure time curve, (d) time trajectory of flame front position, and (e) flame speed of paths $y = 1.8$ m (down) and $y = 0.3$ m (up).

which shows a promotion effect at this time. For small-scale congestion, only promotion is observed. The turbulence formed by the gas flow will cause the flame to accelerate toward the congestion at the initial stage of the indoor explosion. The combustion intensity increases significantly, which changes the overall flame distribution and propagation law in the kitchen. Therefore, the explosion flow field shows greater complexity. The transition process from laminar to turbulent flow in the entire explosion flow field affected by congestion becomes the root cause of the dual-action transformation mechanism.

4.2.2. Characteristics of Flow Field in the Vicinity of Congestion with Different Sizes. Figures 12 and 13 compare the flame combustion rate, turbulent kinetic energy, and gas flow velocity in the vicinity of the refrigerator (configuration 6) and range hood (configuration 7), respectively. Figure 12(a) shows that the combustion rate on the left side of the refrigerator (gauge L-01) rises slowly, and the maximum value is only 0.128 kg/s. The combustion rate at the front (gauge L-02) and on the right side (gauge L-03) of the refrigerator showed a rapid upward trend, with a maximum value that was seven to eight times that of the left side of the

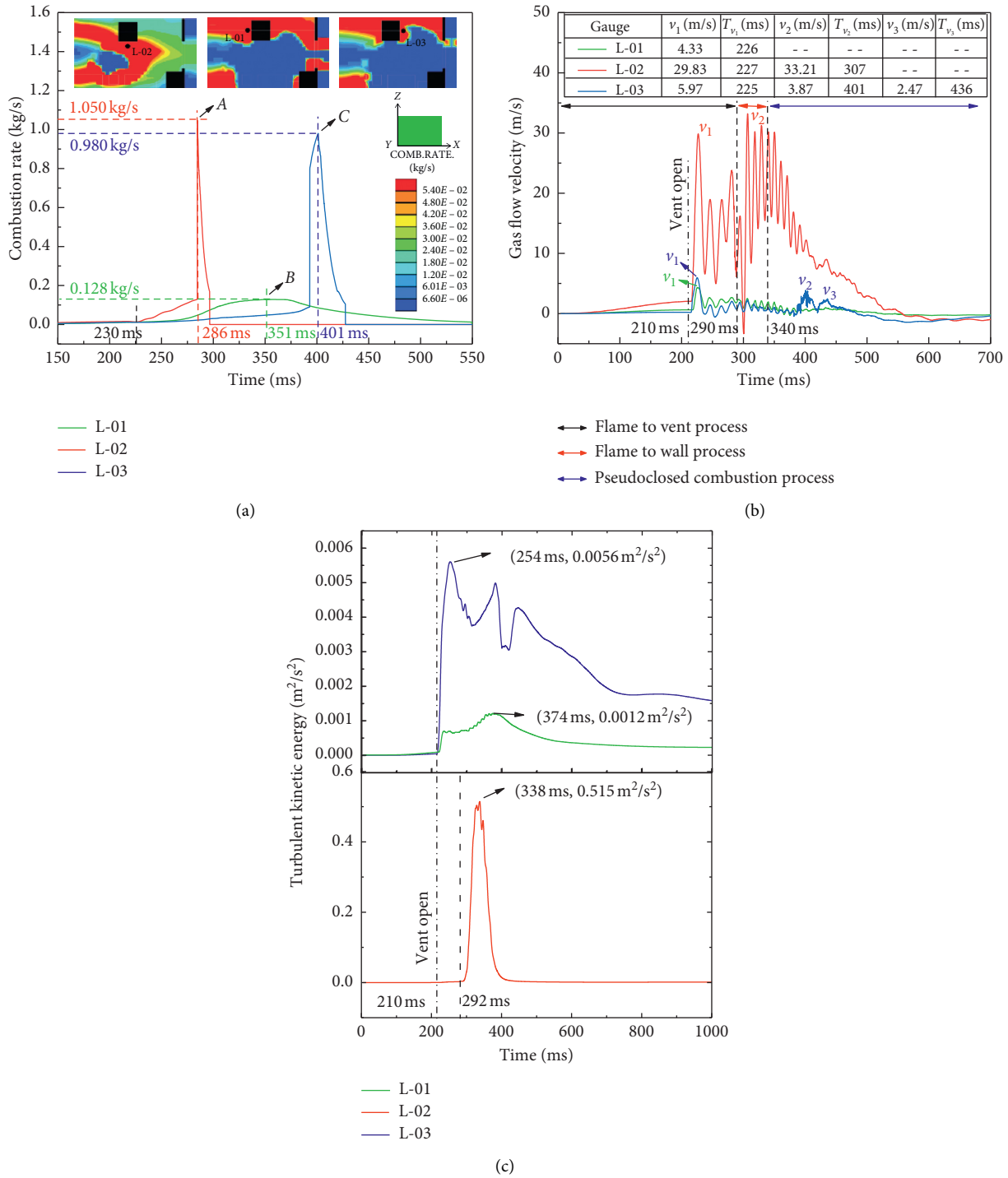

FIGURE 12: Time curve of flow-field parameter change in the vicinity of refrigerator. (a) Combustion rate. (b) Gas flow velocity. (c) Turbulent kinetic energy.

refrigerator, and occurred in different flame propagation stages. The maximum combustion rate at the front of the refrigerator occurs in the flame propagation phase toward the vent, as shown in Figure 12(a)-A. The maximum values on the left and right sides occur in the flame propagation phase and pseudoclosed combustion phase, respectively, as shown in Figures 12(a)-B and 12(a)-C.

Figure 12(b) shows that there are significant differences in the gas flow velocity and number of peak structures around the refrigerator. At the front of the refrigerator, the gas flow velocity was not hindered by the refrigerator, and the first peak v_1 caused by the opening of the vent was five to seven times that of the left and right sides of the refrigerator. Subsequently, owing to the effects of combustion instability

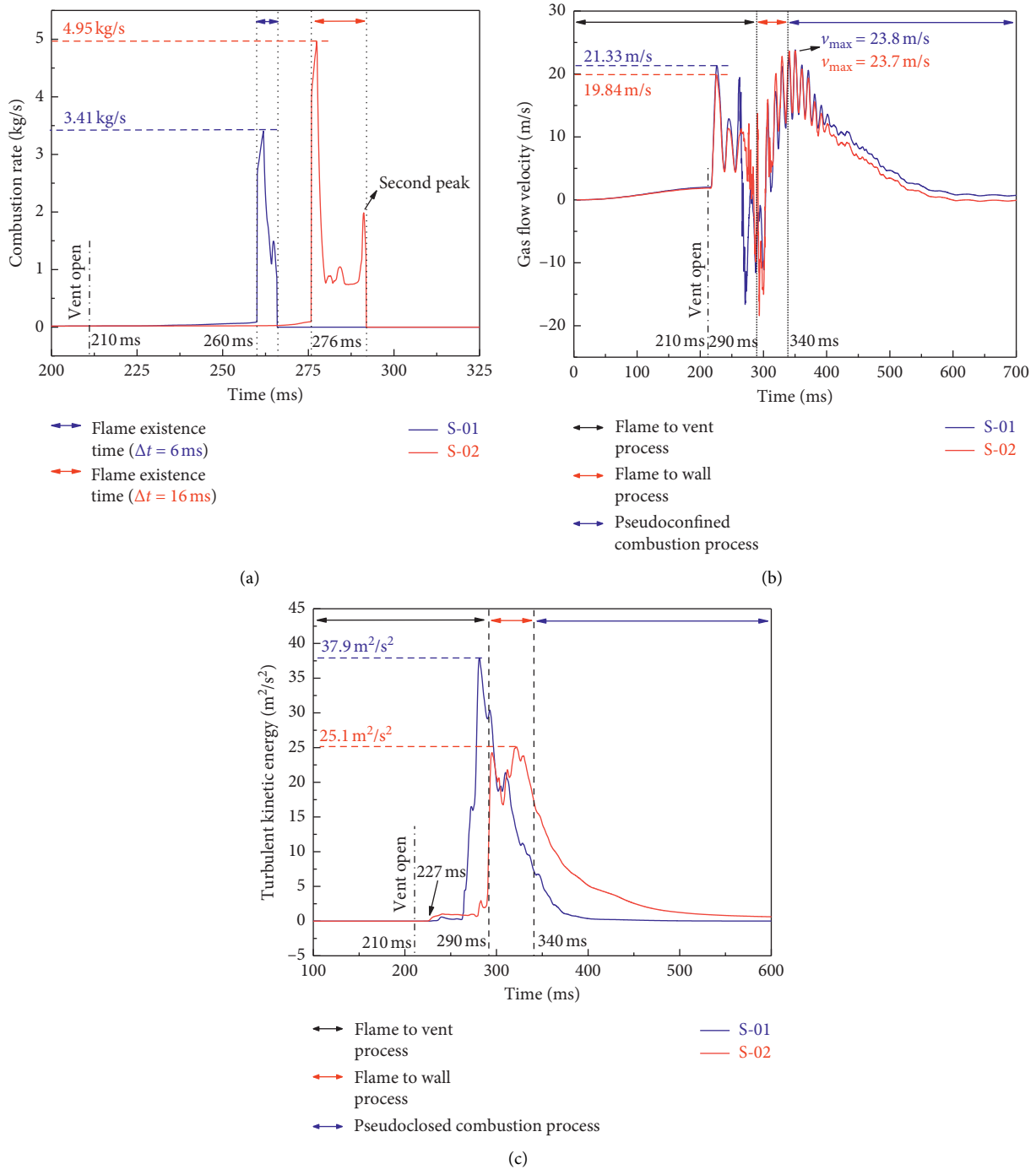

Figure 13: Time curve of flow-field parameter change in the vicinity of range hood. (a) Combustion rate. (b) Gas flow velocity. (c) Turbulent kinetic energy.

and airflow inertia, a series of fluctuations of the airflow speed occurred. It is interesting to note that three gas flow acceleration processes can be observed on the right side of the refrigerator, which lead to the formation of weak peaks v_1 and v_2; these are related to the vortex formed by the gas on the right side of the refrigerator. Figure 12(c) shows that the turbulent kinetic energy at the front of the refrigerator is significantly greater than that on the left and right sides; there are also differences in the development process of turbulent kinetic energy. The turbulent kinetic energy on the right side of the refrigerator has a "three-peak" structure.

As shown in Figure 13(a), the explosion flame first appeared on the side of the range hood (gauge S-01) and then reached the bottom of the range hood (gauge S-02), which is related to the difference in the gas flow velocity in Figure 13(b) and the turbulence formation sequence in Figure 13(c). After

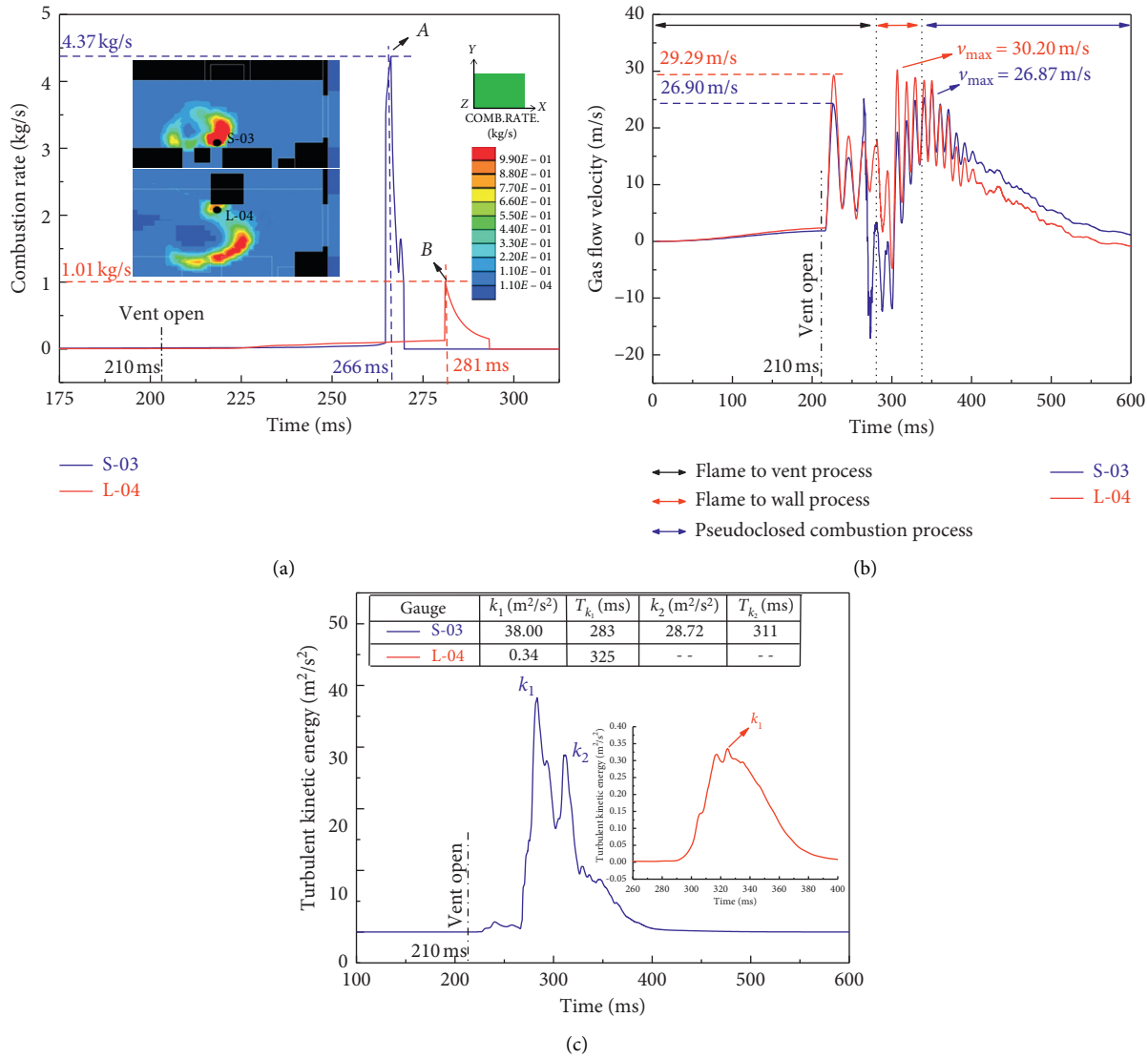

Figure 14: Comparison of flow-field parameters in the vicinity of refrigerator/range hood. (a) Combustion rate. (b) Gas flow velocity. (c) Turbulent kinetic energy.

the vent was opened, the gas velocity peak that formed on the side of the range hood was larger, and turbulence was formed first. The confined space at the bottom of the range hood makes it is easier to retain combustible gas; hence, the combustion rate was higher and the flame burning time was relatively longer ($\Delta t = 16$ ms). The maximum gas velocity in the two places was formed in the pseudoclosed combustion stage, and the difference between the two was small.

Interestingly, the combustion rate and turbulent kinetic energy time curve on the side and bottom of the range hood present a "double-peak" structure. The first peak is related to the arrival of the flame front, and the strong turbulence formed by the flame wake causes the remaining combustible gas to burn further, thus forming the second peak. As seen in Figures 13(a) and 13(c), the change in turbulent kinetic energy after 260 ms always lags behind the change in combustion rate, which indicates that the accelerated burning flame will increase the turbulence in the passing area. Therefore, the turbulence formed by the gas flow near the congestion will accelerate the flame front, and the high-speed flame will form a larger vortex at its tail, which will lead to intensified turbulence. It can be seen that there is a positive feedback mechanism between the burning flame and the turbulence of the flow field.

Figure 14 compares the characteristics of the flow-field parameters in the vicinity of the refrigerator and the range hood (configuration 8). From Figures 14(a)-A and 14(a)-B, the burning flame first appeared near the range hood, and the combustion rate near the range hood was significantly greater than that near the refrigerator. The combustion rate structure near the two congestion sizes was different. Only a single-peak structure was observed near the refrigerator because the turbulence that formed near the refrigerator was lower, and the flame combustion rate was reduced. After the flame passes, it cannot produce a more intense turbulence. Therefore, a second peak will not be formed.

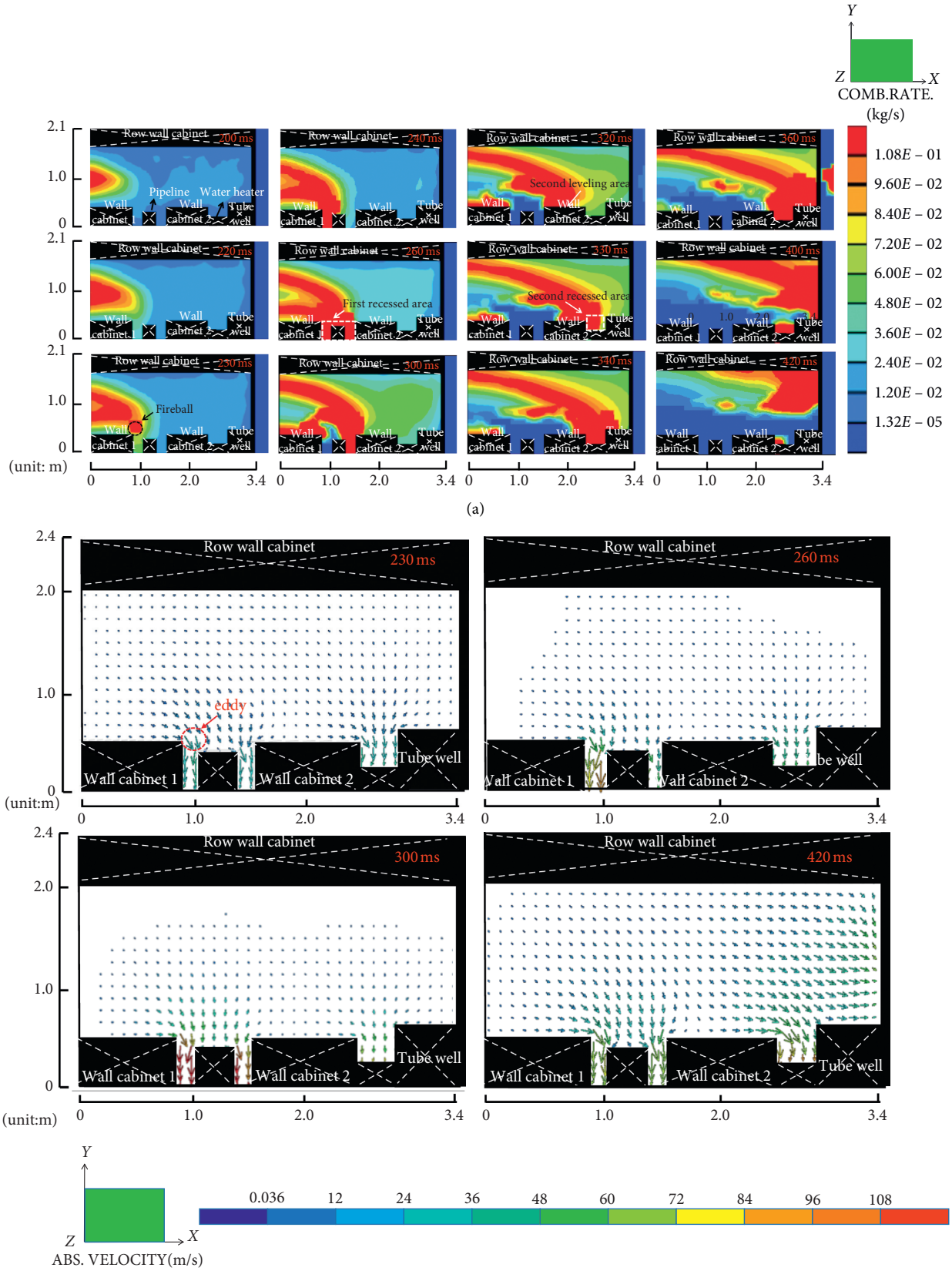

Figure 15: The variation law of (a) flame propagation and (b) flow-field velocity vector on the $z = 2$ m slice after ignition.

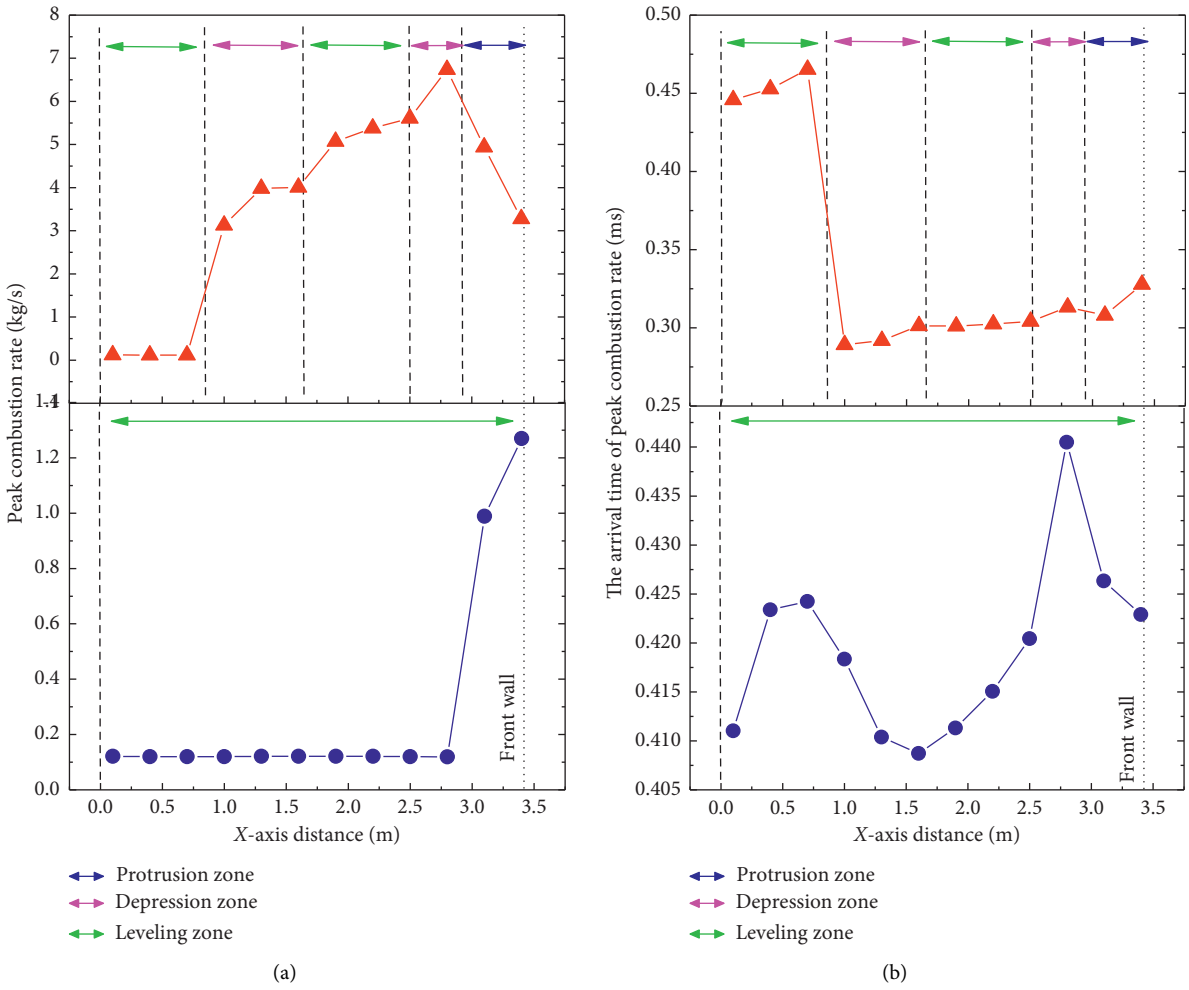

Figure 16: Continued.

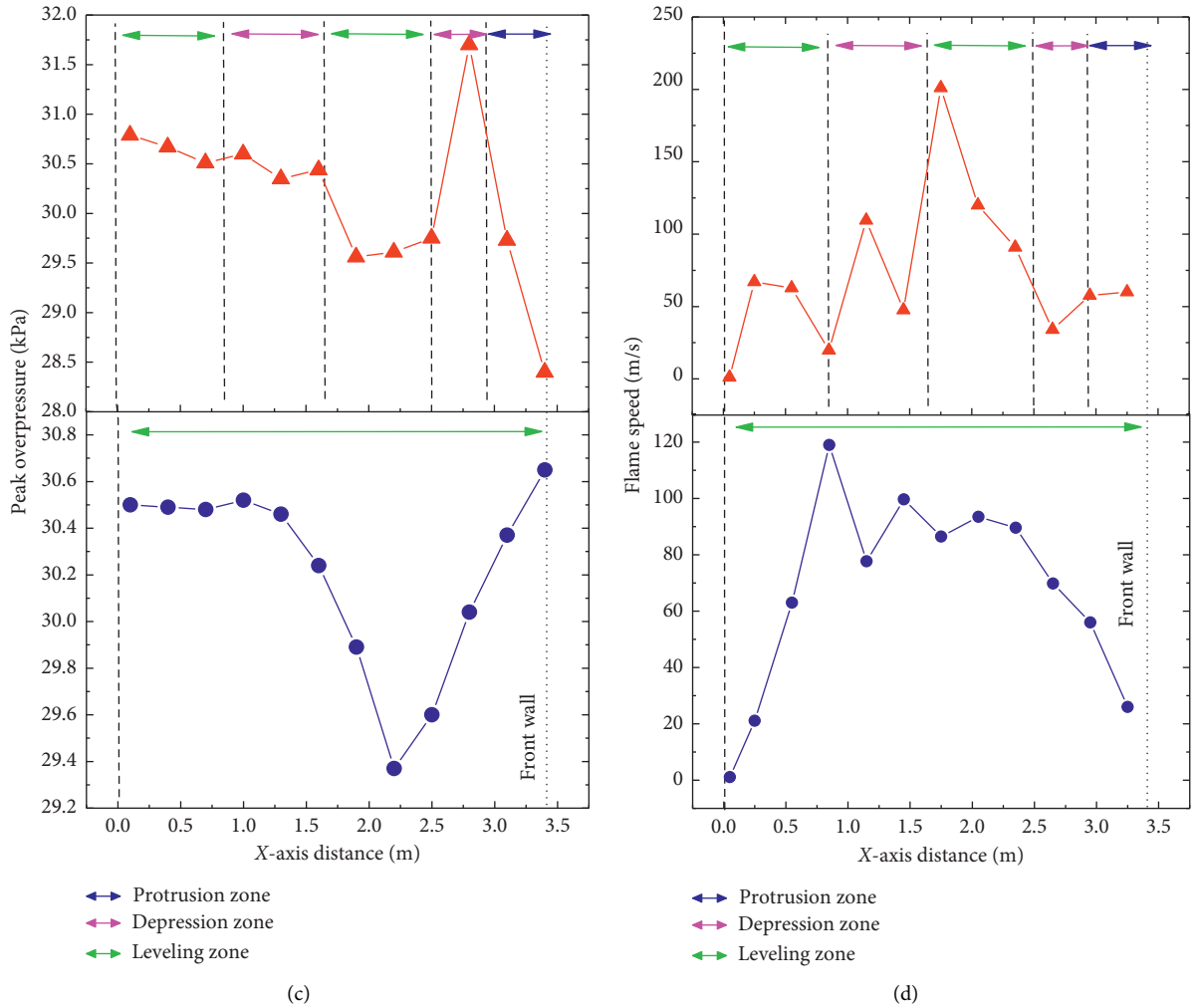

Figure 16: The variation law of (a) peak combustion rate and (b) its arrival time, (c) overpressure time curve, and (d) flame speed of configurations 3 (bottom) and 5 (top) on the $z = 2$ m slice.

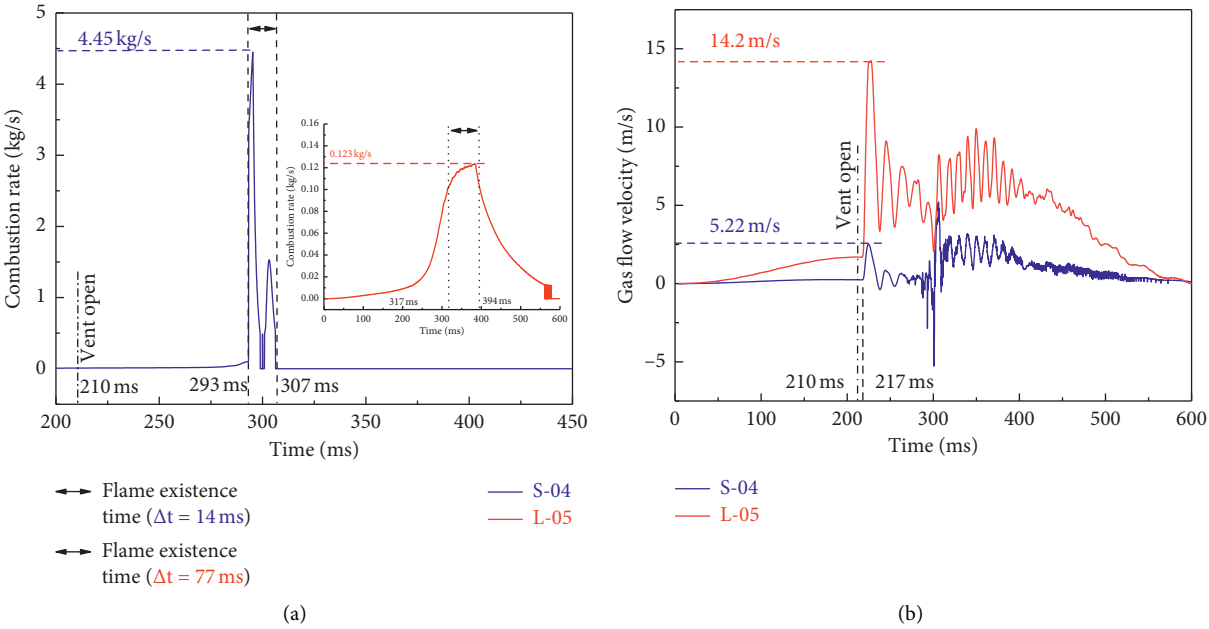

Figure 17: Continued.

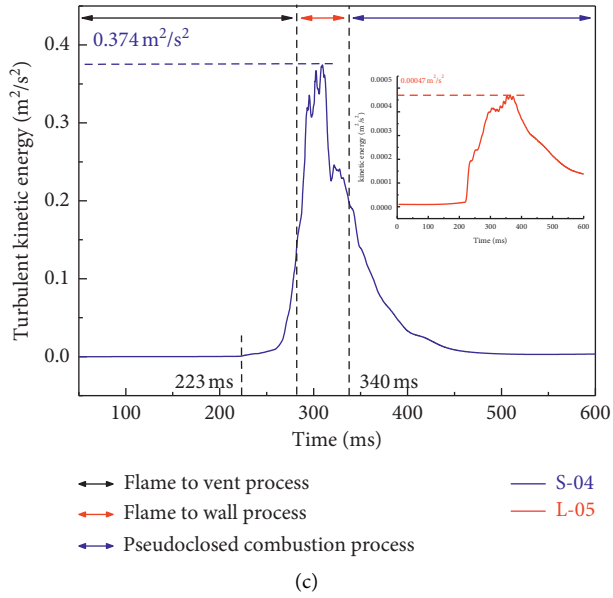

(c)

Figure 17: Comparison of flow-field parameters in the vicinity of congestion of the flat and abrupt cross section. (a) Combustion rate. (b) Gas flow velocity. (c) Turbulent kinetic energy.

Comparison of Figures 14(b) and 14(c) showed that the turbulent kinetic energy generated near the range hood and the refrigerator is very different. The peak turbulent kinetic energy was more than 110 times greater, but the gas flow velocity near the range hood was lower than that of the refrigerator as a whole.

4.3. Influence of Congestion Cross Section on Explosion Flow Field

4.3.1. The Law of Flame Propagation Induced by Characteristics of Congestion Cross Section. To understand the effects of a flat congestion cross section (configuration 3) and an uneven congestion cross section (configuration 5) on the flame structure, Figure 15 shows the combustion rate and flow velocity vector cloud diagram on the $z = 2$ m slice. Moreover, to clarify the quantitative difference of flame propagation, Figure 16 compares (a) the peak combustion rate and (b) its arrival time, (c) overpressure time curve, and (d) flame propagation velocity on the two paths ($y = 1.7$ m, $z = 2$ m; $y = 0.4$ m, $z = 2$ m). Figure 15(a) shows that, compared with the flat side of the congestion, the finger flame front on the concave and convex sides of the cross section began to deform at 220 ms, the combustion rate increased significantly, and a fireball appeared near the first recessed area (230 ms), which is related to the eddy caused by the abrupt change in the cross section in Figure 15(b). With the increase in vortices of various scales, the flow field began to produce turbulence, the combustion rate increased rapidly (Figure 16(a)) after the flame entered the congestion recessed area, and the peak combustion rate arrival time was shortened (Figure 16(b)). At 260 ms, the flame gradually filled the first recessed area, and the flow velocity at 300 ms was further strengthened, exceeding 96 m/s.

Affected by the eddy current induced by the abrupt change of the congestion cross section, the flame speed reached its maximum value after entering the second levelling zone, as shown in Figure 16(d). At the same time, the combustion rate on the path of the cross section mutation continued to increase and reached the maximum value in the second recessed area. This indicates that the continuous cross-sectional mutation caused by the compact arrangement of various kitchen furniture induced a continuous increase in the flame combustion rate. In the recessed area, a relatively long-term continuous burning was induced; hence, the overpressure will be greater. On the flat side of the congestion cross section, no significant changes in the flame shape and combustion rate were observed. This shows that a flat congestion cross section helps to maintain the stability of the flame structure, thereby reducing overpressure.

4.3.2. Characteristics of Flow Field in the Vicinity of Different Cross-Sectional Congestion. The influence of the surface depression and protrusion of the congestion, caused by the continuous arrangement of kitchen furniture, on the explosion flow field is explored in detail. Figure 17 compares the flow field parameters, such as combustion rate, gas flow velocity, and turbulent kinetic energy in the vicinity of the surface of wall cabinet and range hood (configuration 9).

Figure 17(a) shows that the flatness and abrupt change in the congestion cross section will cause significant differences in the flame combustion rate. On the surface of the wall cabinet, which was not affected by the turbulence induced by congestion, the increase and decrease of the combustion rate were slow. However, when subjected to the strong turbulence induced by the cross-sectional mutation, the flame

combustion rate sharply increased at 293 ms. The higher flame propagation speed and burning velocity quickly exhausted the combustible gas, resulting in the flame existing for only 14 ms. It can be seen from Figure 17(b) that the gas flow velocity is greatly affected by the opening of the vent. The flow velocity at the two locations increased significantly at 210 ms. However, the flow velocity in the abrupt cross section was hindered by congestion, and the gas velocity in the direction of the vent was lower overall; even the velocity in the direction of negative pressure appeared. The peaks of the turbulent kinetic energy at the two locations reached a maximum during the flame propagation process toward the wall (Figure 17(c)). The turbulent kinetic energy induced by congestion with an abrupt cross section was significantly greater than that with the flat cross section; this difference could reach up to three orders of magnitude.

5. Conclusions

The CFD method was used to study the natural gas restrained explosion venting process in a typical Chinese civil kitchen. The influence of the scale effect and cross-sectional mutation characteristics of congestion, such as common indoor furniture and electrical appliances, on the explosion flow field was systematically analysed. The main conclusions are as follows:

(1) Under the comprehensive action of asymmetrically distributed congestion, the gas explosion flame in the kitchen appears to undergo uneven burning. The counters and wall cabinets arranged close to the wall and along the flame propagation direction had little effect on the flame shape and speed, while the range hood and water heater have an opposite effect on the explosion flame. There will be an ellipsoidal violent burning zone near such congestion, causing the flame to initially spread on one side of the room and then accelerate and expand to catch up with the flame front. The nonuniform combustion of the flame in the flow field caused more combustible gas to stay in the room and burn violently, which increased the explosion temperature and overpressure.

(2) The typical vented explosion overpressure change process in the kitchen can be divided into five development stages. Stage III is related to the vented gas mass flow, and Stage IV is affected by the combustion rate, mass flow, and flame surface area. The phenomenon of slight overpressure fluctuations in Stage V was caused by pseudoclosed combustion. Four overpressure peaks controlled by different physical processes were identified, and their formation mechanism can be explained by the flame development process.

(3) The characteristics of congestion scale lead to obvious differences in promoting and hindering the explosion flow field, although it can be transformed under certain conditions. Before the flame reached the large-scale congestion (refrigerator), the flame combustion intensity and propagation speed were low, and the peak combustion rate arrival time increased, which has an obstructive effect at this time. As the flame passed through the narrow passage formed by the refrigerator, wall cabinet, and wall, it induced a strong turbulent combustion phenomenon at the rear of the refrigerator, thereby promoting gas combustion and flame propagation. Small-scale congestion, such as range hoods, only promoted the explosion flow field. The phenomenon of pseudoclosed combustion only occurred on the surfaces and gaps of large-scale congestion, such as counters and wall cabinets.

(4) Congestion with abrupt cross sections will result in a significant increase in flame deformation and combustion rate, while congestion with flat cross sections will help maintain the stability of the flame structure. Various vortex scales will be formed in the flow field in the abrupt area of the congestion cross section, and high-speed burning in this area will be induced. The continuous cross-sectional mutations caused by the compact arrangement of different types of kitchen furniture will induce a continuous increase in the combustion rate, and the continuous burning of gas in the recessed area will induce a stronger overpressure. However, there will be no obvious change in the flame shape and combustion rate near the congestion with flat cross sections.

(5) Based on the above conclusions, to effectively prevent natural gas explosion disasters in the kitchen, the following measures are proposed:

(i) Reduce the small-scale furniture and electrical appliances in the kitchen. Small-scale congestion will induce stronger turbulence, causing significant changes in the flame structure, resulting in strong turbulent combustion and strong overpressure disasters.

(ii) Furniture and electrical appliances in the kitchen should be placed close to the wall, and their long sides should be placed as far as possible along the direction of the window and door to reduce narrow spaces and gaps. Reducing the gap between the congestion and wall will not only reduce the turbulence on the flame propagation path but also prevent the occurrence of pseudoclosed combustion.

(iii) Avoid the compact arrangement of furniture and electrical appliances with different cross-sectional dimensions along the direction of the window and door. The continuous cross-sectional mutation of congestion on the flame propagation path will induce strong turbulent

combustion and increase the explosion hazard in the kitchen.

Nomenclature

V: The volume of the room (m^3)
A_v: Vent area (m^2)
V_{ob}: The volume of the congestion (m^3)
k: Turbulent kinetic energy ($m^2 \cdot s^{-2}$)
P_e: Maximum external explosion overpressure (kPa)
d: Axial distribution range of the unburned gas cloud (m)
x: The space coordinate
t: The time coordinate
p: The static pressure
E: Energy (j)
C_V: The constant volume specific heat (j/kg/K)
T: Temperature (K)
m_{fu}: The fuel mass fraction
H_c: Heat of combustion (kj/mol)
C_μ: Constant of k-ε model (m^2/s)
C_1; Constant of k-ε model
C_2:
R_{fu}: Volume combustion rate ($kg/m^3/s$)
R_{min}: Minimum mass fraction
C_t: Dimensionless constant
u_t: Turbulence intensity (m/s)
L_t: Turbulent length scale (m)
S_l: Laminar combustion velocity (m/s)
R_f: Spherical flame radius
F_s: Laminar flame acceleration coefficient

Greeks
$\Gamma*$: Turbulent-diffusion coefficient (m^2/s)
τ_{ij}: Viscous stress tensor
μ_t: Turbulence-viscosity coefficient
ε: Dissipation rate of turbulent kinetic energy (m^2/s^3)
δ_{ij}: The Kronecker δ
ν: Fluid dynamic viscosity (m^2/s)
ρ: Mixture density (kg/m^3)
σ_{sc0}: Quasistatic strengths under uniaxial compression (MPa)
σ_{sttt0}: Quasistatic strengths under uniaxial hydro-tension (MPa)
σ_{st0}: Quasistatic strengths under uniaxial tension (MPa).

Data Availability

The data used to support the findings of this study are available from the corresponding author upon request.

Conflicts of Interest

There are no conflicts of interest regarding the publication of this paper.

Acknowledgments

The authors appreciate the financial support from the National Key R&D Program of China (no. 2017YFC0804700), the Beijing Natural Science Foundation-Municipal Education Committee Joint Funding Project (no. KZ201910017020), the National Natural Science Foundation of China Project (no. 51404029), the Science and Technology Plan Project of Beijing Education Commission (no. KM202010017008), the Beijing Science and Technology Nova Program (no. Z181100006218092), and the Training Funded Project of the Beijing Young Backbone Talents of China (no. 2018000020124G087).

References

[1] P. Li, P. Huang, Z. Liu, B. Du, and M. Li, "Experimental study on vented explosion overpressure of methane/air mixtures in manhole," *Journal of Hazardous Materials*, vol. 374, pp. 349–355, 2019.
[2] L. Pang, Q. Hu, J. Zhao, P. Lv, S. Sun, and K. Yang, "Numerical study of the effects of vent opening time on hydrogen explosions," *International Journal of Hydrogen Energy*, vol. 44, no. 29, pp. 15689–15701, 2019.
[3] Z. Chen, B. Fan, X. Jiang, and J. Ye, "Investigations of secondary explosions induced by venting," *Process Safety Progress*, vol. 25, no. 3, pp. 255–261, 2006.
[4] G. Li, Y. Du, S. Wang, S. Qi, P. Zhang, and W. Chen, "Large eddy simulation and experimental study on vented gasoline-air mixture explosions in a semi-confined obstructed pipe," *Journal of Hazardous Materials*, vol. 339, pp. 131–142, 2017.
[5] D. J. Park, Y. S. Lee, and A. R. Green, "Experiments on the effects of multiple obstacles in vented explosion chambers," *Journal of Hazardous Materials*, vol. 153, no. 1-2, pp. 340–350, 2008.
[6] X. Wen, M. Yu, Z. Liu, G. Li, W. Ji, and M. Xie, "Effects of cross-wise obstacle position on methane-air deflagration characteristics," *Journal of Loss Prevention in the Process Industries*, vol. 26, no. 6, pp. 1335–1340, 2013.
[7] I. O. Moen, J. H. S. Lee, B. H. Hjertager, K. Fuhre, and R. K. Eckhoff, "Pressure development due to turbulent flame propagation in large-scale methane-air explosions," *Combustion and Flame*, vol. 47, pp. 31–52, 1982.
[8] A. J. Harrison and J. A. Eyre, "The effect of obstacle arrays on the combustion of large premixed gas/air clouds," *Combustion Science and Technology*, vol. 52, no. 1-3, pp. 121–137, 1987.
[9] P. A. Diakow, J. K. Thomas, and E. Vivanco, "Comparison of large-scale vented deflagration tests to CFD simulations for partially congested enclosures," *Journal of Loss Prevention Process Industries*, vol. 56, pp. 147–154.
[10] C. R. Bauwens, J. Chaffee, and S. Dorofeev, "Effect of ignition location, vent size, and obstacles on vented explosion overpressures in propane-air mixtures," *Combustion Science and Technology*, vol. 182, no. 11-12, pp. 1915–1932, 2010.
[11] Y. Chen, Z. Li, C. Ji, and X. Liu, "Effects of hydrogen concentration, non-homogenous mixtures and obstacles on vented deflagrations of hydrogen-air mixtures in a 27 m3 chamber," *International Journal of Hydrogen Energy*, vol. 45, no. 11, pp. 7199–7209, 2020.

[12] Q. Zhang, Y. Wang, and Z. Lian, "Explosion hazards of LPG-air mixtures in vented enclosure with obstacles," *Journal of Hazardous Materials*, vol. 334, pp. 59–67, 2017.

[13] G. Tomlin, D. M. Johnson, P. Cronin, H. N. Phylaktou, and G. E. Andrews, "The effect of vent size and congestion in large-scale vented natural gas/air explosions," *Journal of Loss Prevention in the Process Industries*, vol. 35, pp. 169–181, 2015.

[14] T. Skjold, H. Hisken, S. Lakshmipathy et al., "Vented hydrogen deflagrations in containers: effect of congestion for homogeneous and inhomogeneous mixtures," *International Journal of Hydrogen Energy*, vol. 44, no. 17, pp. 8819–8832, 2019.

[15] J. Chao, C. R. Bauwens, and S. B. Dorofeev, "An analysis of peak overpressures in vented gaseous explosions," *Proceedings of the Combustion Institute*, vol. 33, no. 2, pp. 2367–2374, 2011.

[16] W. P. M. Mercx, A. C. van den Berg, C. J. Hayhurst, N. J. Robertson, and K. C. Moran, "Developments in vapour cloud explosion blast modeling," *Journal of Hazardous Materials*, vol. 71, no. 1-3, pp. 301–319, 2020.

[17] Y. Wang, Z. Lian, and Q. Zhang, "Effect of ignition location and vent on hazards of indoor liquefied petroleum gas explosion," *Combustion Science and Technology*, vol. 189, no. 4, pp. 698–716, 2017.

[18] S. Zhang and Q. Zhang, "Effect of vent size on vented hydrogen-air explosion," *International Journal of Hydrogen Energy*, vol. 43, no. 37, pp. 17788–17799, 2018.

[19] L. Pang, Q. Zhang, W. Li, C. Xiang, and R. M. Tan, "Relationship between shock wave and high-temperature flow produced by gas explosion in coal mine roadways," *Chinese Journal of High Pressure Physics*, vol. 25, pp. 457–462, 2011.

[20] B. Angers, A. Hourri, P. Benard, E. Demaël, S. Ruban, and S. Jallais, "Modeling of hydrogen explosion on a pressure swing adsorption facility," *International Journal of Hydrogen Energy*, vol. 39, no. 11, pp. 6210–6221, 2014.

[21] GB50096, *Design Code for Residential Buildings*, Ministry of Housing and Urban-Rural Development of the People' Republic of China, China, 2011.

[22] 14J913-2, *National Building Standard Design Atlas-Residential Kitchen*, China Institute of Building Standard Design & Research, China, 2014.

[23] K. Yang, P. F. Lv, Q. R. Hu, and L. Pang, "Research on synergetic effect of large-scale obstacles and explosion vents on indoor explosion of natural gas," *Journal of Safety Science and Technology*, vol. 14, pp. 21–27, 2018.

[24] G. Ferrara, S. K. Willacy, H. N. Phylaktou et al., "Venting of gas explosion through relief ducts: interaction between internal and external explosions," *Journal of Hazardous Materials*, vol. 155, no. 1-2, pp. 358–368, 2008.

[25] Q. Bao, Q. Fang, Y. Zhang, L. Chen, S. Yang, and Z. Li, "Effects of gas concentration and venting pressure on overpressure transients during vented explosion of methane-air mixtures," *Fuel*, vol. 175, pp. 40–48, 2016.

[26] K. Yang, Q. R. Hu, S. H. Sun, P. F. Liu, and L. Pang, "Research progress on multi-overpressure peak structures of vented gas explosions in confined spaces," *Journal of Loss Prevention Process Industries*, vol. 62, Article ID 103969, 2019.

[27] X. Rocourt, S. Awamat, I. Sochet, and S. Jallais, "Vented hydrogen-air deflagration in a small enclosed volume," *International Journal of Hydrogen Energy*, vol. 39, no. 35, pp. 20462–20466, 2014.

[28] M. Schiavetti and M. Carcassi, "Maximum overpressure vs. H2 concentration non-monotonic behavior in vented deflagration. Experimental results," *International Journal of Hydrogen Energy*, vol. 42, no. 11, pp. 7494–7503, 2017.

[29] V. D. Sarli, A. D. Benedetto, and G. Russo, "Using Large Eddy Simulation for understanding vented gas explosions in the presence of obstacles," *Journal of Loss Prevention Process Industries*, vol. 69, no. 1-3, pp. 435–442, 2009.

[30] C. Xu, L. Cong, Z. Yu, Z. Song, and M. Bi, "Numerical simulation of premixed methane-air deflagration in a semi-confined obstructed chamber," *Journal of Loss Prevention in the Process Industries*, vol. 34, pp. 218–224, 2015.

[31] D. J. Park, Y. S. Lee, and A. R. Green, "Prediction for vented explosions in chambers with multiple obstacles," *Journal of Hazardous Materials*, vol. 155, no. 1-2, pp. 183–192, 2008.

[32] D. J. Park, A. R. Green, Y. S. Lee, and Y. C. Chen, "Experimental studies on interactions between a freely propagating flame and single obstacles in a rectangular confinement," *Combustion and Flame*, vol. 150, no. 1-2, pp. 27–39, 2007.

[33] D. Li, Q. Zhang, Q. Ma, S. Shen, J. Chen, and S. Ren, "Influence of built-in obstacles on unconfined vapor cloud explosion," *Journal of Loss Prevention in the Process Industries*, vol. 43, pp. 449–456, 2016.

[34] H. Phylaktou and G. E. Andrews, "The acceleration of flame propagation in a tube by an obstacle," *Journal of Hazardous Materials*, vol. 85, no. 3-4, pp. 363–379, 1991.

[35] T. Huld, G. Peter, and H. Stadtke, "Numerical simulation of explosion phenomena in industrial environments," *Journal of Hazardous Materials*, vol. 46, no. 2-3, pp. 185–195, 1996.

[36] P. S. Volpiani, T. Schmitt, O. Vermorel, P. Quillatre, and D. Veynante, "Large eddy simulation of explosion deflagrating flames using a dynamic wrinkling formulation," *Combustion and Flame*, vol. 186, pp. 17–31, 2017.

[37] O. Vermorel, P. Quillatre, and T. Poinsot, "LES of explosions in venting chamber: a test case for premixed turbulent combustion models," *Combustion and Flame*, vol. 183, pp. 207–223, 2017.

[38] A. R. Masri, S. S. Ibrahim, N. Nehzat, and A. R. Green, "Experimental study of premixed flame propagation over various solid obstructions," *Experimental Thermal and Fluid Science*, vol. 21, no. 1-3, pp. 109–116, 2000.

[39] R. Hall, A. Masri, P. Yaroshchyk, and S. Ibrahim, "Effects of position and frequency of obstacles on turbulent premixed propagating flames," *Combustion and Flame*, vol. 156, no. 2, pp. 439–446, 2009.

[40] K. Zhang, Z. Wang, L. Ni, Y. Cui, Y. Zhen, and Y. Cui, "Effect of one obstacle on methane-air explosion in linked vessels," *Process Safety and Environmental Protection*, vol. 105, pp. 217–223, 2017.